Impact of the Gravity Field and Steady-State Ocean Circulation Explorer (GOCE) mission on ocean circulation estimates. Volume and heat transports across hydrographic sections.

Jens Schröter, Martin Losch and Bernadette Sloyan

Alfred-Wegener-Institut für Polar- und Meeresforschung, Bremerhaven

Short title: VOLUME AND HEAT TRANSPORTS FROM GOCE

Abstract. Accurate geoids are expected to improve our knowlegde of the dynamic sea surface height (SSH) as a mirror of the dynamic state of the oceans. The dedicated geoid mission GOCE is expected to be lauched in 2004. It will lead to a highly accurate geoid model with a resolution of degree and order 200. We examine the impact of this mission on the assessment of large scale oceanic mass and heat transports via its expected error characteristics. We do so applying a linear box inverse model and a non-linear section inverse model to hydrographic data and to (synthetic) sea surface height data. The results are compared to those obtained when substituting the error estimates of the GRACE mission and the present day geoid EGM96.

For the box inverse model, we find an average reduction in transport uncertainties in Experiment A (which includes model error at the level of sea surface height variability) of about 9% for GRACE geoid error covariances and about 17% for GOCE over the "hydrography only" solution. In both GRACE and GOCE these average percentage improvements are significantly increased when the SSH variability signal is excluded (Experiment B) to 42% for GRACE and 47% for GOCE. We expect a greater improvement in the accuracy of ocean transports from GOCE when WOCE hydrographic data are used to enclose numerous, smaller box regions.

The *a priori* assumptions of the non-linear model about the ocean circulation are much more conservative than for the box model. As a consequence, the uncertainties of large scale transports are much bigger than for the linear model. On the other hand, since this model builds on small scale balances, it can resolve small scale features of the flow field better. SSH data with GRACE geoid error covariances reduce the uncertainties

on the average by 29%, with GOCE geoid error covariances by 37%. Exclusion of the SSH variability changes (Experiment B) these numbers by less than 5% points.

Summarizing our results and those of Part I, III and IV of this study we conclude that the GRACE mission reduces the marine geoid uncertainties such that altimetry becomes useful for the study of the steady state ocean circulation. The GOCE mission will improve the accuracy of the circulation estimates even further on the large scales and introduce higher accuracy on shorter wavelenths as well. Furthermore, it will enable us to study individual ocean currents.

1. Introduction

Estimating the mean ocean circulation is one of the major tasks of physical oceanography. *Wunsch* [1978], and many latter studies [e.g. *Fu*, 1986; *Roemmich and McCallister*, 1989; *Rintoul*, 1991; *Macdonald*, 1998; *Sloyan and Rintoul*, 2001b] provide one approach to determine the mean steady-state circulation. This method uses in-situ measurements along hydrographic sections and employs inverse techniques to obtain an estimate of the large scale flow through those sections. Mean ocean circulation is understood as the average over a long period, i.e. associated with the lowest frequencies. The inverse model then determines a steady state, or stationary, solution which serves as an approximation of the mean flow.

The underdetermination of the linear system used in the oceanographic inverse problem can be reduced by the addition of further independent information. This independent information could be derived from direct ocean measurements including current moorings, Lagrangian floats, tracers and satellite derived sea-surface height measurements. Of all the sources of additional information sea-surface height measurements provide potentially the best resolution and coverage for all ocean regions. With the advent of altimetric data of extraordinary accuracy and precision from the TOPEX/Poseidon or ERS2 mission these measurements are at hand. To this date this information has mostly been used in studies of the time-dependent phenomena in the ocean, e.g. tides [*Le Provost et al.*, 1998; *Egbert*, 1997], where the absolute sea surface height is not needed. For the use of satellite altimetry data in the *steady-state*

ocean problem, one has to reference the altimetric height to a marine geoid in order to determine the mean dynamic sea-surface height. The uncertainties associated with the marine geoid exceed those of the altimetry by an order of magnitude rendering the mean sea-surface height very noisy.

While the present geoid accuracies limit the use of satellite altimetry on the determination the mean ocean circulation, two dedicated satellite missions, which will determine an accurate geoid, are now funded or proposed: Gravity Recovery and Climate Experiment GRACE and; Gravity field and steady-state Ocean Circulation GOCE. Of these two gravity missions GRACE will fly in 2001 and GOCE will fly in 2004 [*Balmino et al.*, 1998]. Given that, in the near future, we will have marine geoid models with finer resolution and increased accuracy it is appropriate at this time to again address some of the issues raised by previous studies (e.g. *Wunsch and Gaposchkin* [1980]; *Ganachaud et al.* [1997]). The new geoid models will in particular extend the range of wavelength with sufficient accuracy to be useful for ocean inverse models. We will study specifically, how this increase in spectral resolution will influence the sea-surface height information in theb context of determination of the steady-state ocean circulation. The work presented here is the second in a series of four articles which studies these questions from different perspectives. Part II evaluates the impact of improved geoid models on the accuracy of ocean mass and heat transport estimates determined from two inverse models. The impact of the geoid is described by its error covariance matrix.

The first model is a linear "box" inverse model similar to that used in

Ganachaud et al. [1997]. It differs by the description of diapycnal fluxes which are modelled expicitely here. Other differences to *Ganachaud et al.* [1997] concern the solution technique. We interpolate the model to the data and use sea surface height instead of sea surface slope as observation. A truncated singular value decomposition is performed for the matrix inversion. Furthermore we use EGM96 geoid [*Lemoine et al.*, 1998] as the state-of-the-art geoid model. For this geoid and that of the GRACE mission we extend the expansion in spherical harmonics from degree and order 25 to degree and order 70. The GOCE geoid model is expanded to degree and order 200.

The box inverse model is applied to the Southern Ocean. Nine high quality hydrographic sections are used to subdivide the Southern Ocean into six regions or "boxes". Simple dynamics and conservation principles allow us to determine an absolute circulation that is consistent with hydrography and water mass analysis. A first set of experiments with the EGM96 geoid exhibits results that are inconsistent with known properties of the large scale circulation. A similar result was reported by *Dobrindt and Schröter* [2001] who found a southward transport of bottom water in the South Atlantic when combining EGM96 geoid and Topex/Poseidon altimetry with a steady state ocean circulation inverse model.

We suspect this results from an under-estimation of the error covariance associated with EGM96. For this reason we will not use the EGM96 geoid model in our calculations, but only its error statistics. Thus, sea surface height (SSH) data to be assimilated in our study are not taken from altimetry but are derived from the inverse model. For the "box" inverse model the SSH data are taken from a previously calculated solution that

is based on hydrographic measurements. Consequently, the surface height is perfectly compatible with the model and the inverse solution does not change by adding the SSH "data". However, the different error estimates for the additional SSH information change the error estimates of the property transports of the inverse model.

The second inverse model is non-linear. Here we use output of an eddy resolving (1/3°) primitive equation general circulation model of the FLAME (Family of Linked Atlantic Model Experiments) group [*Redler et al.*, 1998]). In this case SSH "data" and its error characteristics does change the inverse solution, but we do not have to rely on an inaccurate geoid either. The inverse model models the FLAME "reality" as it would model the real ocean for real measurements.

In both of these inverse models rigorous error analysis is applied to calculate the error covariance matrix of the oceanic mass and heat transports and its dependence on different geoid error estimates. For both models the error covariance of the EGM96, and proposed GRACE and GOCE geoid missions are used. Two sets of experiments are reported. In experiment A we make a very conservative assumption about the error of the inverse models, while in experiment B rather optimistic error levels are assumed.

The paper has the following structure. Firstly we describe how the error covariance of each geoid model is determined for the hydrographic sections. This is similar for both inverse models. The assessment of the different geoid models on the accuracy of mass and heat transport estimates for each inverse model are then described. Finally, the impact shown in both inverse model applications are drawn together in the discussion and compared to other studies.

2. SSH Covariances

The two inverse models we use calculate the most probable solution of a set of dynamical and conservation equations and a set of observations with their statistical error descriptions. In order to combine measurements of different type correctly, these measurements have to be weighted with their respective inverse of the corresponding data error covariance and summed up to form a norm or so-called "cost function" J.

In this task we study the impact of different *a priori* assumptions about the geoid model error, thus its covariance matrix. Three covariances are available: EGM96 [*Lemoine et al.*, 1998] to degree and order $L = 70$; and one estimate each of the geoid covariances for the future mission GRACE; and GOCE (Sneeuw, pers. com.). The latter two are available to degree and order $L = 150$ and $L = 300$, respectively, where they intersect the Kaula curve for the signal variance and where the signal-to-noise ratio becomes 1. However, we chose lower L's, namely 70 for GRACE and 200 for GOCE. These choices correspond to the wavelengths 570 km and 200 km respectively, which the geoid missions are designed to resolve. A cutoff at a low degree and order has also been used by *Ganachaud et al.* [1997] in the same context. Strictly speaking, we are trying to estimate the impact of improved geoid information on the determination of oceanic transports in the same way as it is done in the three dimensional inverse model of the Atlantic Ocean of *LeGrand* [2001]. If we wish to consider how much the flow field of a two dimensional section inverse model or a box-inverse model can be constrained an expansion of the error covariance matrix to higher degree and order

would be appropriate.

Since the sea surface height (SSH) signal $\zeta = h - N$ is the difference between the altimetric measurement h and the reference geoid N, we consider two error contributions to the overall covariance of the signal, the geoid error covariance C_N and a covariance due to measurement errors C_h. The actual sea surface height is not in steady state but it is assumed to fluctuate about a mean state with covariance C_{fluc}. As both models used in this task are steady state models this covariance must be treated as an error about the steady state. Furthermore we assume an uncorrelated measurement error χ. Finally we have to consider the covariance C_m of the so called "model error" or "misrepresentation error", i.e. the principle inability of the model to repoduce the measurement. Therefore we arrive at the covariance to be considered for the signal ζ

$$C_\zeta = C_N + C_m + C_{fluc} + \chi = C_N + C_m + C_h, \tag{1}$$

where the uncorrelated χ is taken to be the estimated error to a mean sea surface height obtained by optimal mapping of a multi-year, multi-satellite data set (LeTraon, pers. com.). C_{fluc} is the error covariance introduced by the time dependence of SSH when it is compared to the surface height of the stationary model. As pointed out by Ganachaud et al. [1997], its specification is a large task and they derive an upper bound for their equivalent error matrix $\mathbf{R_{tt}}$ from the slope spectrum of the surface variability. In a similar approach we calculate the covariance of SSH between TOPEX/Poseidon cross-over points from a five year series (R. Coleman, pers. com.). The model error covariance C_m is very small as the model has no difficulty of producing sea surface

height profiles of any shape. In the following we neglect C_m in comparison with the larger contributions C_N and C_h.

The covariance on the model grid is derived by linear interpolation. We obtain a full matrix that is governed predominantly by the seasonal cycle and to a smaller extent by eddy variability. Note that errors in the altimetric signal due to instrument noise, insufficient removal of barotropic signals (tides, waves, etc.), and erroneous correction terms (ionosphere, wet and dry troposphere, etc.) are all included in this matrix.

We now make the conservative assumption that the error due to time dependence C_{fluc} is given by this variability (Experiment A). Part of the same error is included in the error variance χ which describes how accurate we can estimate a mean sea level in the presence of noise and variability. In a second experiment (B) we optimistically assume all errors are fully accounted for by χ and set C_{fluc} to zero.

In practice the two contributions to ζ have different resolutions. For the geoid this resolution is represented as the maximum degree and order L used and for h it is the resolution of the measurement device. We assume, that the geoid resolution is the limiting factor. For this reason before adding the different covariances, one has to remove all small scales from the altimeter covariance that are not resolved by the geoid. We achieve this synchronization of resolution by applying the same linear low-pass filter as *Ganachaud et al.* [1997]. Let $\phi(x)$ be a function to be filtered, and $f_k(y, x)$ the low-pass filter, then

$$\overline{\phi(x)} = \int f_k(y, x)\phi(y)dy \tag{2}$$

will not contain wave numbers larger than k. In our discrete system we evaluate (2)

using the trapezoidal rule. The equation can then be rewritten in matrix form as:

$$\overline{\phi} = F_k^T \phi. \tag{3}$$

The covariance matrices can be filtered in the same manner:

$$\overline{C(x, x')} = \int \int f_k(y, x) C(y, y') f_k(y', x') dy dy', \tag{4}$$

and in matrix notation:

$$\overline{C} = F_k^T C F_k. \tag{5}$$

Figure 1.

Figure 1 shows the total altimeter covariance $C_h = C_{fluc} + \chi$ along a hydrographic

section across the North Atlantic along 24°N which will be studied below. Also shown

is C_h filtered according to (5) for different cutoff wavelengths corresponding to the

different geoid models used.

Figure 2.

Figures 2 and 3 depict the corresponding error covariance matrices C_N and C_ζ.

Figure 3.

Figure 4 shows the square roots of the diagonal elements of the same matrices and the

Figure 4.

contributions C_N, C_{fluc}, and χ_h.

In order to compare altimeter data with prior knowledge from hydrography we have

to weight the data by its inverse covariance matrix. However, because all small scales

have been removed, the finite sea surface height covariance is rank deficient on a small

scale grid. For that reason we diagonalise it and keep only the non-zero eigenvalues of

the following expansion: If $\mathbf{v}_k$ are the eigenvectors and σ_k^2 the corresponding eigenvalues

of C_ζ, we define the weighting matrix W_ζ as a pseudo-inverse of C_ζ:

$$W_\zeta = \sum_{k=k_{min}}^{k_{max}} \mathbf{v}_k \sigma_k^{-2} \mathbf{v}_k^T, \tag{6}$$

where k_{min} and k_{max} identify the smallest and largest eigenvalue kept in the expansion. The effect of this procedure becomes apparent when one examines the cost function term for sea surface height (see also equations 13 and 17).

$$\begin{aligned} J_\zeta &= \frac{1}{2}(\zeta - \zeta^*)^T W_\zeta (\zeta - \zeta^*) \\ &= \frac{1}{2} \sum_{k=k_{min}}^{k_{max}} \left(\frac{\zeta_k - \zeta_k^*}{\sigma_k} \right)^2 \end{aligned} \tag{7}$$

with $\zeta_k = \mathbf{v}_k^T \cdot \zeta$ and $\zeta_k^* = \mathbf{v}_k^T \cdot \zeta^*$ being the coefficients of the expansion of the modeled sea surface height ζ and sea surface height data ζ^*, respectively, into the eigenvectors of C_ζ. Thus, only the "eigenshapes" of the covariance matrix that are distinguishable from numerical noise are fitted. Figure 5 shows the SSH that is actually "seen" by the model, that is its representation by the eigenvectors of the covariance matrix

$$\zeta^{(r)} = \sum_{k=k_{min}}^{k_{max}} \zeta_k \mathbf{v}_k. \tag{8}$$

Also shown are the misfits $\zeta^* - \zeta^{(r)}$. For EGM96 and GRACE this representation can describe the large structures of the data, while for GOCE it also resolves the finer scales at the western end of the section (Figure 5).

Figure 5.

In both inverse models, the model SSH ζ is diagnosed from the geostrophic surface velocity by integration

$$\zeta(x) = \int_0^x \frac{f}{g} v(x', z = 0) dx' \tag{9}$$

where $v(x', z = 0)$ is the surface velocity normal to the section, f the coriolis parameter and g the acceleration due to gravity.

The calculation of the weighting matrix W_ζ which was presented above for the section at 24°N is repeated separately for all nine sections of the box-inverse model. This way we arrive at a total weighting matrix for SSH which is block diagonal, i.e. small correlations which exist between the different sections are neglected in our calculations.

3. Sensitivity analysis using a linear box inverse model of the Southern Ocean

3.1. Inverse Model

3.1.1. Inverse model description   A box inverse model, following that of *Wunsch* [1978], is designed. Mass, heat and salt are conserved in all layers. Two novel additions to the inverse model used in this study are the inclusion of independent diapycnal flux unknowns for each property and the explicit inclusion of air-sea fluxes of heat, freshwater, momentum (wind), and the water mass transformation they drive [*Sloyan*, 1997; *Sloyan and Rintoul*, 2001a].

The inclusion of independent diapycnal fluxes for each property represents the net diapycnal flux which results from all mixing processes that act to transfer mass, heat or salt between water masses in the ocean interior *Sloyan and Rintoul* [2001a]. (Here "interior" is taken to mean the entire ocean beneath the sea surface. Diapycnal fluxes across isopycnals outcropping in the surface mixed layer, for example, are included

in the interior diapycnal fluxes). These mixing processes include advection, diffusion, cabelling and eddy fluxes.

Exchange of heat and freshwater with the atmosphere results in net buoyancy forces which can transfer fluid from one density layer to another *Walin* [1982]. To date, inverse methods have not explicitly included these effects on the mass, heat or salt conservation equations. Inverse models usually either down-weight the conservation requirement in layers that outcrop and interact with the overlying atmosphere, or only consider conservation below the thermocline *Metzl et al.* [1990]; *Rintoul* [1991]; *Macdonald* [1998]; *Ganachaud and Wunsch* [2000]. Rather than discard the information contained in the conservation constraints for outcropping layers, it is desirable to include the effects of air-sea interaction explicitly. This is particularly so at high latitudes, where many layers outcrop. More importantly, the diapycnal fluxes driven by air-sea interaction are a fundamental part of the three-dimensional circulation of the ocean. An inverse model which seeks to determine this circulation should include these processes in a physically-consistent manner.

The effect of air-sea fluxes of heat, freshwater and momentum can be included explicitly in the model following the strategy of *Walin* [1982]; *Tziperman* [1988]; *Schmitt et al.* [1989] and *Speer and Tziperman* [1992]. The data sets used to calculate the air-sea fluxes contain errors, including errors in the bulk formulae used and a lack of oceanographic and meteorological observations, especially at high latitudes and over subtropical regions away from commercial shipping routes [*Speer and Tziperman*, 1992; *Barnier et al.*, 1995]. As a result, we treat these climatologies as an initial guess

in the inverse model, and use the inverse solution to determine corrections to the climatological data sets which make them consistent with the hydrographic data and the model physics. A complete description of the method, the derived corrections to the air-sea fluxes, and the water mass formation driven by the air-sea fluxes can be found in *Sloyan and Rintoul* [2001a, b].

The conservation equation, for a layer bounded by neutral density surfaces h_m and h_{m+1}, including the diapycnal flux unknowns for each property and the air-sea flux driven transformations, has the form:

$$
\begin{aligned}
\sum_{j=1}^{M} & \left[\Delta x_j \int_{h_m}^{h_{m+1}} C_j (v_r + v_{ref})_j dz + E_j C_j \right] \\
& + (w_c A C)_m - (w_c A C)_{m+1} \\
& + (F_c + F_c^*)_m - (F_c + F_c^*)_{m+1} = 0.
\end{aligned}
\tag{10}
$$

Here Δx_j is the station spacing at pair j, C_j is the property value per unit mass at this pair. The geostrophic shear velocity v_{r_j} is determined from the hydrographic data, $E_j C_j$ is the Ekman property flux at pair j and F_c is the total flux across an outcropping isopycnal driven by buoyancy forcing.

The resulting system of conservation equations can be written in matrix form as

$$
\mathbf{Ab} + \mathbf{n} = \mathbf{d}
\tag{11}
$$

$\mathbf{A}$ is a matrix whose elements are the area $\times$ property concentration C at each station pair in each layer, and for each layer interface; $\mathbf{d}$ is the property divergence in each layer due to relative $(\Delta x_j \times C_j v_{r_j})$ and Ekman $(E_j C_j)$ fluxes, and $\mathbf{b}$ is the vector of unknowns which consist of the reference level velocities v_{ref_j}, the diapycnal property

fluxes ($w_c = w_m, w_h, w_s$) and corrections to the air-sea climatologies F_c^*. $\mathbf{n}$ is the model noise. In this linear system generally the unknowns outnumber the equations leading to an underdetermined problem with an infinite number of solutions. Here we overcome this underdetermination by seeking a Gauss-Markov [*Wunsch*, 1996] estimate of the solution to (11):

$$\mathbf{b} = \mathbf{C_{bb}}\mathbf{A}^T(\mathbf{A}\mathbf{C_{bb}}\mathbf{A}^T + \mathbf{C_{nn}})^{-1}\mathbf{d} \tag{12}$$

where the noise $\mathbf{C_{nn}}$ is the *a priori* covariance of the model and $\mathbf{C_{bb}}$ the *a priori* covariance of the solution. $\mathbf{b}$ and $\mathbf{n}$ are assumed to be uncorrelated (see e.g. *Wunsch* [1996] for a discussion of a Gauss-Markov estimate). The Gauss-Markov estimate minimizes the variance of both the model noise n and the solution b which is equivalent to a maximum likelyhood estimate or to minimizing the following cost function

$$J = \frac{1}{2}\mathbf{n}^T\mathbf{C_{nn}}^{-1}\mathbf{n} + \frac{1}{2}\mathbf{b}^T\mathbf{C_{bb}}^{-1}\mathbf{b}. \tag{13}$$

The posterior error covariance or uncertainty of the solution estimate $\mathbf{b}$ about its true values is

$$\mathbf{P} = \mathbf{C_{bb}} - \mathbf{C_{bb}}\mathbf{A}^T(\mathbf{A}\mathbf{C_{bb}}\mathbf{A}^T + \mathbf{C_{nn}})^{-1}\mathbf{A}\mathbf{C_{bb}}. \tag{14}$$

It is independent of the value of the divergences $\mathbf{d}$ or the solution $\mathbf{b}$ (12). Instead it it fully given by the specification of the model in matrix form (11) and by the prior error covariances $\mathbf{C_{nn}}$ and $\mathbf{C_{bb}}$. Variances of different fluxes ϕ reported below are directly calculated from $\mathbf{P}$. For this we expand ϕ in a Taylor series

$$\phi = \phi_0 + \frac{\delta\phi}{\delta b}b = \phi_0 + \hat{L}b \tag{15}$$

where $\hat{L}$ is a linear operator (in case of a scalar observable ϕ it is a vector, $\hat{l}$). This operator describes the sensitivity of ϕ to variations in b. For a linear model higher order terms in (15) are zero. As the box model is based on the balance of fluxes $\hat{l}$ is easily calculated from matrix $\mathbf{A}$. The variance σ_ϕ^2 is then given by

$$\sigma_\phi^2 = <\phi - \phi_0, \phi - \phi_0> = <\hat{l}b, \hat{l}b> = \tilde{l}^T \mathbf{P}\hat{l} \tag{16}$$

where the brackets $<,>$ denote the expectation operator.

3.1.2. Hydrographic data, domain and *a priori* constraints Nine hydrographic sections are used to define six "boxes" in the southern hemisphere oceans, as shown in figure 6. The sections used are recent (1984-1994) high quality hydrographic sections, apart from the I18 section, which was occupied in 1976 (Table 1). The sections across the Pacific, in Drake Passage and south of Australia are part of the WOCE data set. Twenty three layers are chosen to span the water masses in the model domain. The layers are defined by neutral density surfaces calculated using the *Jackett and McDougall* [1997] algorithm.

Across the zonal sections (SAVE2, SAVE4, I18, I32 and P32) the initial reference level is the boundary between the northward flowing Antarctic Bottom Water (AABW) and southward flowing North Atlantic Deep Water (NADW), Indian Deep Water (IDW) and Pacific Deep Water (PDW). In the Argentine basin of SAVE4 and the three

Figure 6.

Table 1.

Southern Ocean choke point sections (DP, SA and SR3) the initial reference level is taken to be the deepest common depth at each station pair.

Following *Rintoul* [1991] model mass uncertainties is given as 0(1-2)Sv, temperature and salt uncertainties are given as a function of layer temperature and salt (anomaly). Therefore, the temperature uncertainty are largest in the surface layers and decrease with depth, while the salt uncertainly is a function its anomaly from the mean salt content. Diapycnal uncertainties are $0(10^{-5}ms^{-1})$ for outcropping neutral surface, $0(10^{-7}ms^{-1})$ for interior surfaces and $0(10^{-6}ms^{-1})$ for undercropping neutral surfaces. The initial air-sea fluxes are given an uncertainty of approximately 50%. *Ganachaud* [2000] used an eddy-permitting ocean general circulation model of the North Atlantic to estimate (mass) errors that could be applicable to inverse methods. This study suggests the mass error applied in our model may be somewhat optimistic.

Table 2 contains information on the *a priori* constraints applied to the inverse model.

Table 2.

3.2. General Circulation - a five layer description

A description of the net meridional and zonal fluxes (Table 3) is given below. This is provided to familiarize the reader with the gross circulation features of the model. The reader is referred to Sloyan and Rintoul (2001a and 2001b) for a thorough description of the Southern Ocean circulation of the model. The errors provided for the Southern Ocean "box" inverse model represent the formal errors of the inverse method - the error associated with determining the reference velocity, and diapycnal fluxes. These formal

errors do not take into account errors due to the asynoptic data, solution sensitivity to the first guess and ocean variability. As the formal errors do not include these other error sources they are unlikely to reflect the true uncertainty in the estimates. In recognition of the inadequacy of the formal error bars, *Macdonald and Wunsch* [1996] and *Macdonald* [1998], for example, chose to increase the uncertainty of all their heat flux estimates by a somewhat arbitrary ± 0.25 PW (based on *Holfort* [1994] error analysis in the South Atlantic). They believed this value more accurately accounted for the effect of (the unmeasured) oceanic variability. The value used is much larger than the formal error bar provided by the inverse method. Here we have chosen to present the estimates with the formal error bars, so that it is clear what the error bars represent. If a good estimate exists of the uncertainty introduced by error sources not included in the formal error bars (e.g. Holfort's value of 0.25 PW for the South Atlantic), this value should be added to the error bars shown here.

Table 3.

Subtropical Atlantic   Across the Atlantic there is a small net southward flux of mass and salt which corresponds to the leakage of Pacific water through Bering Strait and into the North Atlantic Ocean (Table 3). Southward flow North Atlantic Deep Water is balanced by northward thermocline and intermediate water and Antarctic bottom water. The $-18 \pm 4 \times 10^6 \ m^3 s^{-1}$ [1] overturning agrees well with previous estimates [*Dickson and Brown*, 1994; *Rintoul*, 1991; *McCartney*, 1993]. In this study the overturning is closed by a northward flux of upper waters, predominantly

---

[1] 1 Sv = 1 Sverdrup = $10^6 \mathrm{m}^3\mathrm{s}^{-1}$.

by intermediate water. Other authors divide the northward return equally between thermocline and intermediate water [*Macdonald*, 1998].

The balance of the deep Atlantic overturning circulation by upper waters results in a northward heat flux across the Atlantic which in this study we estimate as 0.37 ± 0.05 PW at SAVE4 and 0.49 ± 0.06 PW at SAVE2. The norhward heat flux at SAVE4 is smaller than recent estimates of 0.49 ± 0.25 PW at 27°S by *Macdonald* [1998] and 0.5 ± 0.1 PW at 30°-40°S of *Saunders and King* [1995].

Subtropical Indian In the Indian Ocean there is a southward mass flux at 18°S and 32°S of $7.40 \pm 4 \times 10^6 \ m^3 s^{-1}$ and $8.14 \pm 4 \times 10^6 \ m^3 s^{-1}$, respectively (Table 3). The increase in mass flux between I18 and I32 is not significant and in the limits of the *a priori* model noise of O(1 Sv).

In this model the Mozambique channel between 13°S and 26°S is closed. *Stramma and Lutjeharms* [1997] find a southward transport of 5 Sv in the Mozambique channel and a southward transport of 35 Sv east of Madagascar. *Sætre and da Silva* [1984] suggest that the Mozambique Current is, if at all, only a minor tributary of the Agulhas current. They even question the concept of a continuous Mozambique current. *Macdonald* [1998] resolves the Mozambique channel in her global inverse model and finds no significant flow in the channel. More recently *Ganachaud and Wunsch* [2000] estimate a southward transport of 14 ± 6 Sv across the southern end of the Mozambique channel. *Fu* [1986] estimates a southward transport of 6 Sv in the Mozambique channel. Although the closure of the Mozambique channel is an undesirable feature of this model, zero mass transport is consistent with previous transport estimates.

The size of the Indonesian Throughflow is not constrained by the inverse model. The southward mass flux through the Indian Ocean in this model is within reasonable agreement of all previous estimates of the size of the Indonesian Throughflow including the more recent results of Gordon et al. (1999).

The model exhibits a deep overturning circulation which is weaker than that presented by *Toole and Warren* [1993], but stronger than *Robbins and Toole* [1997] and *Macdonald* [1998]. The overturning circulation is contained to below 1500 dbars resulting in a southward heat flux of -0.79 ± 0.14 PW at 32°S. At the same section *Macdonald* [1998] estimates -1.30 ± 0.28 PW, and *Toole and Warren* [1993] estimate a southward flux of -1.67 PW.

Subtropical Pacific   Across 32°S in the Pacific Ocean there is a net northward transport of $7.31 \pm 3 \times 10^6 \ m^3 s^{-1}$. This results from a net northward flux of thermocline layers, while the strong northward flow of lower deep and bottom water is balanced by southward flow of upper deep water.

The heat flux across 32°S of 0.36 ± 0.13 PW is larger than *Macdonald* [1998]'s heat flux estimates of -0.04 ± 0.32 PW at 28°S and 0.26 ± 0.28 PW at 43°S.

Southern Ocean   In the Southern Ocean the Antarctic Circumpolar Current (ACC) dominates the three meridional sections with an eastward mass flux of $137.5 \pm 7 \times 10^6 \ m^3 s^{-1}$ at Drake Passage, $138.5 \pm 7 \times 10^6 \ m^3 s^{-1}$ south of Africa and $146.7 \pm 7 \times 10^6 \ m^3 s^{-1}$ south of Australia (Table 3). These transports are approximately $5 \times 10^6 \ m^3 s^{-1}$ smaller than the corresponding estimates of *Macdonald* [1998]. The differences arise because at Drake Passage, *Macdonald* [1998] places a transport

contraint on the ACC. In this model no transport constraint is placed on the ACC.

The property divergences between the choke point sections result from imports or exports across the three southern subtropical sections and changes to the water layer composition between the choke point sections. The largest divergences occur between south of Africa and south of Australia. The increases in eastward property fluxes south of Australia result from the inclusion of Indonesian Throughflow water in the Indian sector and their eastward transport with the ACC.

3.3. Impact of Geoid on accuracy of ocean transports

The summary of the circulation presented above shows that the net transports are generally consistent with our current understanding of the circulation of the Southern Ocean. In the following this solution is denoted NOSSH. We now focus on the improvement in the accuracy of those transports that may result from the inclusion of sea surface height (SSH) data derived from satellite altimeters. We assess this impact through three different SSH error covariances. The different error covariance result from the use of the EGM96, and proposed GRACE and GOCE geoid error covariances.

Figure 7.

Figure 8.

Figure 9.

As explained in Section 2, the total SSH error covariance is the sum of the geoid error covariance and the error covariance due to measurement error and fluctuations of the SSH about the mean ocean state. In this study the measurement error is taken from the estimated error to a mean sea surface height (LeTraon, pers. com.) and the fluctuation error covariance is estimated from a five year time series of TOPEX/POSEIDON cross-over data (Coleman, pers com). In this section we show

Figure 10.

Figure 11.

Figure 12.

results for each geoid error covariance (EGM96, GRACE and GOCE, also used to denote the corresponding result) in two experiments. In experiment A we include the variability of the signal C_{fluc} in the SSH error covariance. The second case, experiment B, the variability signal is assumed to be zero and removed from the SSH error covariance.

Fig. 7 and Fig. 8 show that there is a steady improvement in the accuracy of the integrated mass and heat transports of EGM96 over NOSSH, GRACE over EGM96, and GOCE over GRACE for experiment A. The average percentage improvement, for most sections, for each geoid model over the NOSSH solution for mass and heat is: EGM96 5% and 3%; GRACE 9% and 9% and GOCE 18% and 15%, respectively. The increase in the accuracy at the South Atlantic section (SAVE 4) is limited for all geoids. The South Atlantic is relatively well constrained by *a priori* information (Table 2) and therefore the inclusion of extra information via the altimeter sea surface height constraint has a smaller impact on the uncertainty of the transports at this section. A comparison between Fig. 7 and Fig. 9 and, Fig. 8 and Fig. 10 shows that removal of the sea surface height variability from the SSH covariance results in a dramatic improvement in the accuracy of both GOCE and GRACE.

The similar error reduction for the integrated basin-scale property transports between GRACE and GOCE suggests that both geoids have a similar skill in reducing the uncertainty associated with the large-scale ocean transports.

This study is particularly interested in the improved accuracy of small scale oceanic features. Of primary interest are strong currents and their associated transports. The analysis made above for basin-scale transports is repeated for four strong currents in the

Southern Ocean. Fig. 11 and Fig. 12 shows the increase in accuracy of the mass and heat transports associated with selected currents in the southern oceans: the Malvinas and Agulhas currents, the East Australian Current (EAC) and the Sub-Antarctic Front (SAF). Again there is a dramatic increase in the accuracy of the mass transports associated with these currents from experiment A to experiment B. The Malvinas and Agulhas currents, which are relatively wide, show the greatest improvement. Also of significance is the improvement in the Malvinas current for GRACE and GOCE geoid models even though this current has addition *a priori* information from current moorings. The smaller scale SAF show the greatest difference between the accuracy of GRACE and GOCE (experiment B) reflecting the smaller scale resolution of GOCE.

4. Sensitivity analysis using a non-linear section inverse model for the Atlantic Ocean

4.1. Pseudo-Data

Due to absence of a high precision geoid to which actual altimetric sea surface height data can be referenced, we choose an artificial data set complete with temperature, salinity, 3-D velocities, and sea surface height on a regular grid. The data set was obtained from the FLAME (Family of Linked Atlantic Model Experiments) 1/3° North Atlantic Model (NAM) [*Redler et al.*, 1998]. This general circulation model (GCM) is spun up from initial conditions based on 1/4° horizontal resolution annual mean potential temperature and salinity fields [*Boyer and Levitus*, 1997] for a period of 10

years with a surface forcing derived from *Barnier et al.* [1995]. The data set contains snapshots of the model at time intervals of three days. For our purposes the model output is considered as "reality". This is very convenient since in contrast to the real ocean this "model reality" is very well sampled. Therefore, we can compare the results of the inverse model, which is an estimate of the flow field, to the flow field of the FLAME "model reality". The degree of resemblance of the FLAME model output to the real Atlantic Ocean is rather good to our belief but will not be discussed here.

Figure 13.

Figure 14.

From this data set we extract a synoptic snapshot at 24°30'N, approximately along the cruise path of the WOCE Section A5 (see figure 13). This provides us with hydrography and sea surface height data that are consistent within the dynamics of the FLAME model. The FLAME data are interpolated to the grid of the inverse model. After interpolation the instantaneous net volume transport through the section for the snapshot is $\phi_V = 0.06$ Sv, the one year mean $\overline{\phi_V} = 0.28 \pm 3.31$ Sv, the instantaneous heat transport relative to 0°C is $\phi_H = 0.58$ PW and its one year mean value $\overline{\phi_H} = 0.61 \pm 0.12$ PW. The uncertainties of the mean transports are estimated from the standard deviation of the one year record. Figure 14 shows the temporal average of the spatial power spectrum of the one year SSH record and the same for the vertically integrated mass and heat transports, the quantities of interest in this study. It can be seen that most of all three signals consists of wavelengths that can be resolved by the GOCE mission (up to approximately 200 km), and that GRACE (smallest wavelengths resolved are approximately 500 km) is insufficient to resolve important parts of the spectrum.

4.2. Inverse Scheme

4.2.1. Description of the model   We use a nonlinear model based on the finite difference inverse model described in *Nechaev and Yaremchuk* [1995] and further developed in *Yaremchuk et al.* [1998]. Following the standard "assimilation philosophy", we consider all the data as a kind of spatio-temporal sample of a "random" ensemble of the ocean states. Treating the large-scale steady state of the model ocean as an average over this ensemble it is possible to find an approximation to this mean under the assumption that the prior probability distribution is Gaussian. In addition to that, a number of conservation laws and dynamical relationships must be satisfied. These include geostrophy, hydrostatics and a non-linear equation of state for sea water. Furthermore the linearized potential vorticity balance and advective property balances are assumed to be in steady state. Finally an integral kinematic constraint imposes a net mass transport across the section. The latter three of these constraints are imposed in a "weak" form, i.e. they are to be satisfied only within certain error bounds defined by *a priori* statistical assumptions, whereas geostrophy and the equation of state are satisfied exactly. The finite difference model is based on three-dimensional grid boxes in the section plane. On the western end of the section (Gulf Stream region) the along section spacing of these boxes coincides with the grid size of the FLAME (1/3°) model; in the deep sea regions it increases to 1°. The across section width of the boxes is the average of the along section width. In the vertical, the vertices of the boxes are also defined by the uneven GCM grid.

After specifying the probability distribution and the dynamical constraints, we invert the data by seeking the most probable state of the North Atlantic on our model grid under the assumption that the dynamical constraints are satisfied. The numerical technique for that procedure is well established [e.g. *LeDimet and Talagrand*, 1986]. The prior probability density function is proportional to $\exp(-J)$ where the argument J has the the form of the following quadratic cost function:

$$
\begin{aligned}
J = \frac{1}{2}\Bigg\{ &\sum_{m,n}(\hat{I}C_m - C_m^*)^T W_{mn}(\hat{I}C_n - C_n^*) \\
&+ (\zeta - \zeta^*)^T W_\zeta(\zeta - \zeta^*) \\
&+ (\mathbf{u} - \mathbf{u}^*)^T W_{\mathbf{u}}(\mathbf{u} - \mathbf{u}^*) \\
&+ F_w^T W_w F_w + (F^w)^T W^w F^w + (\phi_V - \phi_V^*)^T W_{\phi_V}(\phi_V - \phi_V^*) \\
&+ \sum_n [F_n^T W_{F_n} F_n + (\hat{S}_F F_n)^T D_{F_n}(\hat{S}_F F_n)] \\
&+ (\hat{S}_c C_n)^T D_n(\hat{S}_c C_n) + (\hat{S}_u \mathbf{u})^T D_{\mathbf{u}}(\hat{S}_u \mathbf{u}) \Bigg\}
\end{aligned}
\tag{17}
$$

The first three terms in J attract the solution to the data. C_n^* stands for the measured values of the nth property component (C_1 = temperature, C_2 = salinity), ζ^* identifies the sea surface height data, and $\mathbf{u}^*$ are measurements of horizontal velocities, where they are available. W_{mn}, W_ζ, and $W_{\mathbf{u}}$ are the inverse covariance matrices accounting for the prior statistical structure of the hydrographic properties C_n, the sea surface height ζ and the horizontal velocity field $\mathbf{u}$. In the case of sea surface height, this matrix contains among other errors the error structure of the geoid to which real data would have been referenced (see section 2).

The remainder of the cost function is aimed at diminishing the "errors" in the determination of various components of the unknown steady state. Therefore we assume *a priori* that all arguments in the last seven quadratic functions are statistically independent and have zero means. The different contributions describe: uncertainty of the deviation of the net transport ϕ_V normal to the section from the data value ϕ_V^*, uncertainties of the vertical velocity at the bottom F_w and at the surface F^w, deviations F_n of the property conservation equation from the steady advective balance and finally variances of the grid-scale components of C_n, F_n and $\mathbf{u}$ (smoothness of the fields). The latter are represented by applying the differential operator $\hat{S}_\psi := \partial_{xx} + \nu_\psi(z)\partial_{zz}$, where ν_ψ depends on the field ψ. Following *Yaremchuk et al.* [1998] we choose weights that decrease the grid scale variances to 30% of their first guess values.

To find the maximum of the probability distribution we minimize the cost function J. This optimization problem is solved iteratively using the adjoint method. The adjoint code necessary for this method was generated by the Tangent and Adjoint Model Compiler (TAMC) [*Giering*, 1997; *Giering and Kaminski*, 1996].

4.2.2. Prior Covariances/Variances   Special attention should be drawn to the determination of the inverse covariances W_{mn}, W_ζ, $W_{\mathbf{u}}$, W_{ϕ_V}, W_w, W^w, W_{F_n}, D_n, D_{F_n}, and $D_{\mathbf{u}}$. These quantities define "physically acceptable" deviations of the state vector components from their steady state geostrophically balanced counterparts. In other words, both W and D values should be inversely proportional to the squared amplitudes of the appropriate fields generated by ageostrophic motions and measurement errors. We assume that these fields all are statistically homogeneous in time and, with the exception

of W_{mn}, also in the horizontal. The obvious exception to this is W_ζ (see section 2). A further assumption about the "sub-grid" fields is that they are uncorrelated in space and time.

In general, estimating the prior inverse covariances has been made in accordance with the scheme outlined in *Yaremchuk et al.* [1998], therefore only the major differences in the approach used here are described. The first difference in formulation is the use of additional off-diagonal elements in the tracer covariance function $C_{m,n}(z, z')$. We include vertical cross-correlations, since the vertical spacing of the grid resolves the scales of mesoscale eddies, which are treated as noise by the assimilation scheme. The second difference is that these covariance functions were also assumed to be inhomogeneous along the section in order to account for east-west variations in hydrographic fields. The covariances have been estimated by a Gaussian-bell-shaped running average over the along section coordinate of the section. In order to be able to invert the covariance matrix, an estimate of "ocean noise" according to *Bindoff and McDougall* [1994] has been added to the diagonal. The net mass transport weight has been chosen to be $W_{\phi_V} = 1/10 \text{ Sv}^{-2}$ according to the annual variations of the transport (see section 4.1). The heat transport is not constrained. The weighting matrix for the sea surface height data term is described in section 2.

After the careful definition of J the minimization routine M1QN3 of the MODULOPT library [*Gilbert and Lemaréchal*, 1989] was applied. The minimizer uses a Quasi-Newton algorithm with variable storage (BFGS). It searches for the optimal state in the space of control variables $X = \{C_n, \ \mathbf{u}(z = -H), \ F_w, \ F^w\}$.

4.2.3. Posterior variances Variances of all integral quantities shown in tables 4 in section 4.3 were computed through linear transformations of the error covariance matrix $\mathbf{P}$ between the control variables. This covariance matrix can be identified as the inverse of the Hessian matrix $\mathbf{H}$ associated with the assimilation scheme [*Thacker*, 1989]. Any observable ϕ can be approximated by an expansion around the optimal state of the control variables (15) but now $\hat{l}$ is non-trivial. Its numerical code can be obtained from the TAMC [*Giering*, 1997].

Following the standard approach [*Thacker*, 1989], we assume that the posterior statistics are also Gaussian and fluctuations around the optimal state are small in the sense that the original dynamics are well approximated by the linearized equations. Then the error variance of ϕ is then given by

$$\sigma_\phi^2 = \hat{l}^T \mathbf{H}^{-1} \hat{l}, \tag{18}$$

which is equivalent to (14). As the number of control variables was fairly large (of order 10^4), it is computationally prohibitive to calculate $\mathbf{H}$ and especially $\mathbf{H}^{-1}$. However it is possible to calculate the product of the Hessian matrix $\mathbf{H}$ with any vector [*LeDimet and Talagrand*, 1986]. This enables us to use a polynomial approximation of the property $\psi = \mathbf{H}^{-1/2}\hat{l}$ from which $\sigma_\phi^2 = \langle \psi, \psi \rangle$ can be obtained. This procedure is described in detail by *Yaremchuk and Schröter* [1998]. The software was provided by the authors.

4.3. Results

Mean climatological surface stresses and their standard deviations are taken from *Trenberth et al.* [1990] to calculate the Ekman velocities and Ekman transports using an Ekman depth of 40 m corresponding to a vertical turbulent diffusion coefficient of $A_V = 10^3 \text{cm}^2/\text{s}$, likewise the vertical component of the wind stress curl is used to compute the Ekman pumping into the geostrophic interior of the flow field.

Table 4.

All salinity and temperature values of the selected instantaneous subset of the "data" were used to constrain the model. To simulate the dense sampling of the most prominent small scale feature of the section, the Gulf Stream through Florida Strait, nine velocity measurements (three each at three different depth levels) from that region constrain the flow field even further. For the sea surface height we assumed the two different situations outlined in Section 2. In experiment A we included the variability of the signal C_{fluc} into the SSH error covariance as described in Section 2 to account for the assumption of stationarity of the system. In the second case we assumed zero variability as one would have if one had a time stepping model that could resolve the evolution of the oceanic fields. The optimistic error assumptions of this experiment B mimic the realistic perspective that by the time the GOCE data will be available, computers will be much more powerful than today and therefore the by nature computationally expensive time dependent inverse models will be much more commonly used.

In each experiment, four inverse runs were performed, one with hydrography data alone, labeled NOSSH, and three runs with sea surface heigh data, one for each

geoid error covariances, labeled EGM96, GRACE, and GOCE. There is also a further control run where we assumed "perfect data", that is the error of the sea surface height "measurements" are taken to be 1 mm and uncorrelated. From this run the largest possible impact of SSH data can be estimated.

Table 4 lists the integral mass transport ϕ_V and heat transport ϕ_H (relative to 0°C) through the section for all runs. The content of the table is summarized in Figures 15 and 16. Figures 18 and 19 show the model SSH.

The model without assimilation of SSH data (NOSSH) reproduces the FLAME model reality (reference) to a reasonable extent, however in many details it exhibits significant differences to FLAME. In general, it tends to broaden the narrow Gulf Stream. The resulting increase in northward mass transport to 30 Sv is compensated by a decrease of the northward flow between 282° and 285°E and an increase of the southward flow further east (figure 17). The inversion does not lead to an improved error estimate of total mass transport.

In the unrealistic case of "perfect" SSH data the agreement between model solution and FLAME reference is very good, although the flow field still cannot be reproduced perfectly. For example, the southward deep flow of the abyssal circulation at 285°E is too weak. Obviously, the simple dynamics of the inverse model are only an approximation to the more complex dynamics of FLAME. Nevertheless, the run PERFECT yields an upper limit for the possible improvement of the transport estimates. From Table 4 one can see, that even "perfect" data can improve the *a priori* error estimate of the total mass transport over that of NOSSH by only 3% while the error reduction for

Figure 15.

Figure 16.

Figure 17.

Figure 18.

Figure 19.

the unconstrained heat transport is 75%. The transport errors in the Gulf stream are reduced only by approximately 50%, since here the flow field is already constrained by velocity measurements.

When the SSH data is included with the larger error estimates of EGM96, GRACE and GOCE the error reductions are of course smaller than in the case of "perfect" data. The comparatively well known total mass transport error cannot be improved significantly in any run. The error reduction over the NOSSH for the other transports run are small for EGM96 (between 10% to 20%), considerably larger for GRACE (20% to 38%) and largest for GOCE (between 30% and 45%). The errors are more reduced for the total heat transport than for the Gulf Stream mass and heat transports for the reasons described above. Also the error reduction is, as anticipated, larger for the smaller *a priori* error estimates in experiment B (without the variability of the ocean signal included as an error), but not by very much (less than 10%). The exception in the GRACE runs can be explained as follows: The model can react nonlinearly to changes in the cost function, so that in experiment A the solutions obtained for EGM96 and GOCE are very different compared to that of GRACE. This can be seen from the significantly different transport values for this run (Table 4) and from the flow field in Figure 17. There the GRACE solution exhibits a broadened and intensified Gulf Stream, a too strong northward flow between 282 and 284°E and a strong southward flow in-between. Therefore, because the model is non-linear, the posterior error estimates are different for different solutions.

5. Discussion

We now compare the results of our two inverse models and those of the Atlantic inverse of *LeGrand* [2001]. Our findings from the inverse "box" model (Section 3) and the section finite difference model (Section 4) show differences in the estimated impact of the GOCE geoid model. These differences were expected according to the different concepts of the inverse models. The box inverse model relies on basin scale conservation of mass and other properties, while the finite difference inverse Atlantic of *LeGrand* [2001] and section models are balanced locally on $1° \times 1°$ boxes defined by the model grid. Thus there is a large difference in the resolution of the box and finite difference inverse models. The large scale resolution of the inverse box model is accurately determined by both GRACE and GOCE geoid models, while the smaller resolution of the finite difference inverse models are able to resolve the different accuracy between GRACE and GOCE at these small scales.

At present the large "boxes" defined by hydrographic sections, as used in Section 3, limit the assessment of the improvement in accuracy of ocean transport of GOCE over GRACE geoid models. This will change with the use of hydrographic sections collected during WOCE. The use of WOCE data to define ocean regions will result in smaller, more numerous boxes. The finer resolution of the boxes in a WOCE inverse box model should show a much greater improvement in the accuracy of ocean transport determined using GOCE over those provided from GRACE.

The structure of the improved accuracy provided by GOCE is similar in both finite

difference inverse models of *LeGrand* [2001] and Section 4 but the magnitude of the improvement is smaller in the finite difference section model (Section 4). The difference in the magnitude of the improvement achieved by GRACE is due to differences in the calculation of the geoid error covariance between Part I and Part II. In *LeGrand* [2001], the GRACE error covariance is calculated to degree/order 150 to match the inverse model's resolution. On these high degrees GRACE is rather inaccurate. Because the spherical harmonics are orthogonal only on the sphere, strictly speaking there is alway a leakage of high degree signal (and error!) to low degrees thus increasing the errors of the longer wavelengths. The smaller improvement of GOCE over GRACE shown between the finite difference section inverse over that given in the full Atlantic model reflect the differences in the implied accuracy of GRACE between this study and *LeGrand* [2001]. We would like to stress this difference as it points to a more general problem of representing the marine geoid and sea-surface height (see, e.g.,*Rapp et al.* [1996]).

6. Conclusions

We estimate how an accurately known geoid will lead to improvements in error estimates of large scale oceanic mass and heat transports. This is shown in a box inverse model that is based on hydrographic measurements and a non-linear inverse model based on numerical model (FLAME) "data". In both cases the data are augmented with satellite altimetry of varying accuracy: that of the present day geoid EGM96; and estimates of the performances of the GRACE and GOCE missions.

With each inverse model we ran two experiments (Experiment A and B) for each

geoid model. In experiment A the sea surface height (SSH) or signal ζ error covariance matrix used is the sum of the geoid model error covariance, cross-correlated sea-surface height variability and uncorrelated measurement error. In experiment B the variability signal is removed from the SSH error covariance.

A preliminary experiment with the EGM96 geoid and TOPEX/POSEIDON SSH data resulted in a South Atlantic circulation that was inconsistent with our knowledge of the circulation of this ocean. This suggests that present day geodetic information (i.e. EGM96) does not provide useful information in the determination of large scale oceanic transports. *Ganachaud et al.* [1997] arrived at a similar conclusion using the JGM-3 geoid model.

The second conclusion of this report concerns the improvement in geoid accuracy by the GRACE and GOCE missions. With the inverse "box" model, we find an average reduction of transport uncertainties in Experiment A (inclusion of variability signal) of about 9% for GRACE geoid error covariances and 17% for GOCE over the "hydrography only" solution. In both GRACE and GOCE these average percentage improvements are significantly increased when the SSH variability signal is excluded (Experiment B) to 42% for GRACE and 47% for GOCE. The similar improvement provided from both GRACE and GOCE is a result of the large scale balance which applies in the inverse box model. It is expected that a greater improvement in the accuracy of ocean transports will be provided by GOCE with a box inverse model that uses WOCE hydrographic sections to enclose smaller ocean regions.

In addition we applied a fully non-linear inverse model to hydrographic data of a

single section. The *a priori* assumptions about the ocean circulation of this model are much more conservative than for the box model. As a consequence, the uncertainties of large scale transports are much bigger than for the linear model. SSH data with GRACE geoid error covariances reduce these uncertainties on the average by 29%, with GOCE geoid error covariances by 37%. Exclusion of the SSH variability changes these numbers by less than 5 percent points.

The experiments indicate, that new satellite missions that result in high precision, high resolution geoids will improve estimates of large scale integral properties of the ocean circulation, and significantly improve estimates of oceanic properties over the current geoid EGM96. The improvement of GOCE over GRACE is relatively small for large scale properties but, especially for short scales properties like the transport through Florida Strait we can infer that GOCE will lead to far better estimates than GRACE.

References

Balmino, G., F. Perosanz, R. Rummel, N. Sneeuw, H. Sünkel, and P. Woodworth, European views on dedicated gravity field missions: GRACE and GOCE, An Earth Sciences Division Consultation Document, ESA, ESD-MAG-REP-CON-001, 1998.

Barnier, B., L. Siefridt, and P. Marchesiello, Thermal forcing for a global ocean circulation model using a three-year climatology of ECMWF analyses, *J. Mar. Syst.*, *6*, 363–380, 1995.

Bindoff, N. L., and T. J. McDougall, Diagnosing climate change and ocean ventilation using hydrographic data, *J. Phys. Oceanogr.*, *24*, 1137–1152, 1994.

Boyer, T. P., and S. Levitus, Objective analyses of temperature and salinity for the word ocean on a 1/4 degree grid, *Tech. Rep. NOAA Atlas NESDIS 11*, U.S. Gov. Printing Office, Washington, D.C., 1997.

Dickson, R. R., and J. Brown, The production of North Atlantic Deep Water: Sources, rates and pathways., *J. Geophys. Res.*, *99*, 12,319–12,341, 1994.

Dobrindt, U., and J. Schröter, An adjoint ocean model using finite elements: An application to the south atlantic, *Journal of Atm. Oc. Tech*, 2001, in press.

Egbert, G., Tidal data inversion: Interpolation and inference, *Progress in Oceanography*, *40*, 53–8, 1997.

Fu, L.-L., Mass, Heat and Freshwater fluxes in the South Indian Ocean, *J. Phys. Oceanogr.*, *16*, 1683–1693, 1986.

Ganachaud, A., Large scale oceanic circulation and fluxes of freshwater, heat, nutrients and oxygen, Ph.D. thesis, MIT/WHOI, 2000.

Ganachaud, A., and C. Wunsch, Improved estimates of global ocean circulation, heat transport and mixing from hydrographic data, *Nature*, *408*, 453–457, 2000.

Ganachaud, A., C. Wunsch, M.-C. Kim, and B. Tapley, Combination of TOPEX/POSEIDON data with a hydrographic inversion for determination of the oceanic general circulation and its relation to geoid accuracy, *Geophysical Journal Int.*, *128*, 708–722, 1997.

Giering, R., *Tangent linear and Adjoint Model Compiler , Users manual 1.2*, 1997.

Giering, R., and T. Kaminski, Recipes for Adjoint Code Construction, *Tech. Rep. 212*, Max-Planck-Institut für Meteorologie, 1996.

Gilbert, J. C., and C. Lemaréchal, Some numerical experiments with variable-storage quasi-Newton algorithms, *Mathematical Programming*, *45*, 407–435, 1989.

Holfort, J., Grossraumige Zirkulation und meridional Transporte im Südatlantik, Ph.D. thesis, Institut für Meereskunde an der Christian-Albrechts-Universität Kiel, 490, 1994, in German, English abstract.

Jackett, D., and T. J. McDougall, A Neutral Density variable for the Worlds Oceans, *J. Phys. Oceanogr.*, *27*, 237–263, 1997.

Le Provost, C., F. Lyard, J. Molines, M. Genco, and F. Rabilloud, A hydrodynamic ocean tide model improved by assimilating a satellite altimeter-derived data set, *J. Geophys. Res.*, *103*, 5513–5529, 1998.

LeDimet, F.-X., and O. Talagrand, Variational algorithms for analyses and assimilation of meteorological observations: Theoretical aspects, *Tellus*, *38A*, 97–110, 1986.

LeGrand, P., Impact of the gravity field and steady-state ocean explorer (GOCE) mission on ocean circulation estimates. volume fluxes in a climatological inverse model of the Atlantic, *Journal of Geophysical Research, this issue*, 2001.

Lemoine, F. G., et al., The development of the joint NASA GSFC and National Imagery and Mapping Agency (NIMA) geopotential model EGM96, *Tech. Rep. NASA/TP—1998-206861*, National Aeronautics and Space Administration and Goddard Space Flight Center, 1998.

Macdonald, A. M., The global ocean circulation: a hydrographic estimate and regional analysis, *Prog. Oceanogr.*, *41*, 281–382, 1998.

Macdonald, A. M., and C. Wunsch, An estimate of the global ocean circulation and heat flux, *Nature*, *382*, 436–439, 1996.

McCartney, M. S., Crossing of the Equator by the Deep Western Boundary Current in the western Atlantic Ocean, *J. Phys. Oceanogr.*, *23*, 1953–1974, 1993.

Metzl, N., B. Moore, and A. Poisson, Resolving the intermediate and deep advective flows in the Indian Ocean by using temperature, salinity, oxygen and phosphate data: the interplay of biogeochemical and geophysical tracers, in *Geochemical*

Variability in the Oceans, Ice and Sediments, edited by L. P. Labeyrie and C. Jeandel, vol. 89 of *Palaogeography, Palaeoclimatology, Palaeoecology (Global and Planetary Change Section)*, pp. 81–111, Elsevier Science,, 1990.

Nechaev, D. A., and M. I. Yaremchuk, Application of the adjoint technique to processing of a standard section data set: World Ocean Circulation Experiment section S4 along 67°S in the Pacific Ocean, *J. Geophys. Res.*, *100*, 865–879, 1995.

Rapp, R. H., C. Zhang, and Y. Yi, Analysis of dynamic ocean topography using TOPEX data and orthonormal functions, *J. Geophys. Res.*, *101*, 22,583–22,598, 1996.

Redler, R., K. Ketelsen, J. Deng, and C. Böning, A high-resolution numerical model for the circulation of the Atlantic Ocean, in *Proceedings in the Fourth European SGI/CRAY MPP Workshop*, edited by H. Lederer and F. Hertweck, pp. 95–108, 1998.

Rintoul, S. R., South Atlantic interbasin exchange, *J. Geophys. Res.*, *96*, 2675–2592, 1991.

Robbins, P. E., and J. M. Toole, The dissolved silica budget as a constraint on the meridional overturning circulation of the Indian Ocean, *Deep-Sea Res.*, *Part A*, 879–906, 1997.

Roemmich, D., and T. McCallister, Large scale circulation of the North Pacific Ocean, *Prog. Oceanogr.*, *22*, 171–204, 1989.

Sætre, R., and A. J. da Silva, The circulation of the Mozambique Channel, *Deep-Sea Res.*, *Part A*, 485–508, 1984.

Saunders, P. M., and B. R. King, Oceanic Fluxes on the WOCE A11 Section, *J. Phys. Oceanogr.*, *25*, 1942–1957, 1995.

Schmitt, R. W., P. S. Bogden, and C. E. Dorman, Evaportaion minus Precipitation and density fluxes for the North Atlantic, *J. Phys. Oceanogr.*, *19*, 1208–1221, 1989.

Sloyan, B. M., The circulation of the Southern Ocean and the adjacent ocean basins determined by inverse methods, Ph.D. thesis, Institute of Antarctic and Southern Ocean Studies, University of Tasmania, 1997.

Sloyan, B. M., and S. R. Rintoul, The Southern Ocean limb of the global deep overturning circulation, *J. Phys. Oceanogr.*, *31*, 143–173, 2001a.

Sloyan, B. M., and S. R. Rintoul, Circulation, renewal and modification of Antarctic mode and intermediate water, *J. Phys. Oceanogr.*, *31*, 1005–1030, 2001b.

Speer, K., and E. Tziperman, Rates of Water Mass Formation in the North Atlantic Ocean, *J. Phys. Oceanogr.*, *22*, 93–104, 1992.

Stramma, L., and J. R. E. Lutjeharms, The flow field of the subtropical gyre of the South Indian Ocean, *J. Geophys. Res.*, *102*, 5513–5530, 1997.

Thacker, W. C., On the role of Hessian matrix in fitting models to data, *J. Geophys. Res.*, *94*, 6177–6196, 1989.

Toole, J. M., and B. A. Warren, A hydrographic section across the Subtropical South Indian Ocean, *Deep-Sea Res.*, *40*, 1973–2019, 1993.

Trenberth, J. M., J. Olson, and W. G. Large, The mean annual cycle in Global Ocean wind stress, *J. Phys. Oceanogr.*, *20*, 1742–1760, 1990.

Tziperman, E., Calculating the time-mean oceanic general circulation and mixing coefficient from hydrographic data, *J. Phys. Oceanogr.*, *18*, 519–525, 1988.

Walin, G., On the relation between sea-surface heat flow and thermal circulation in the ocean, *Tellus*, *34*, 187–195, 1982.

Wunsch, C., The North Atlantic general circulation west of 50° determined by inverse methods, *Reviews of Geophysics and Space Physics*, *16*, 583–620, 1978.

Wunsch, C., *The Ocean Circulation Inverse Problem*, Cambridge University Press, Cambridge, New York, Melbourne, 1996.

Wunsch, C., and E. M. Gaposchkin, On using satellite altimetry to determine the gerneral circulation of the oceans with application to geoid improvement, *Reviews of Geophysics and Space Physics*, *18*, 725–745, 1980.

Yaremchuk, A. I., and J. Schröter, Spectral analysis of symmetric operators: Application to the Laplace tidal model, *Journal of Computational Physics*, *147*, 1–21, 1998.

Yaremchuk, M., D. Nechaev, J. Schröter, and E. Fahrbach, A dynamically consistent analysis of circulation and transports in the southwestern Wedell Sea, *Annales Geophysicae*, *16*, 1024–1038, 1998.

This manuscript was prepared with AGU's LATEX macros v5, with the extension package 'AGU^{++}' by P. W. Daly, version 1.6b from 1999/08/19.

Figure Captions

C_h, unfiltered

C_h, filtered, λ_c = 570 km

C_h, filtered, λ_c = 200 km
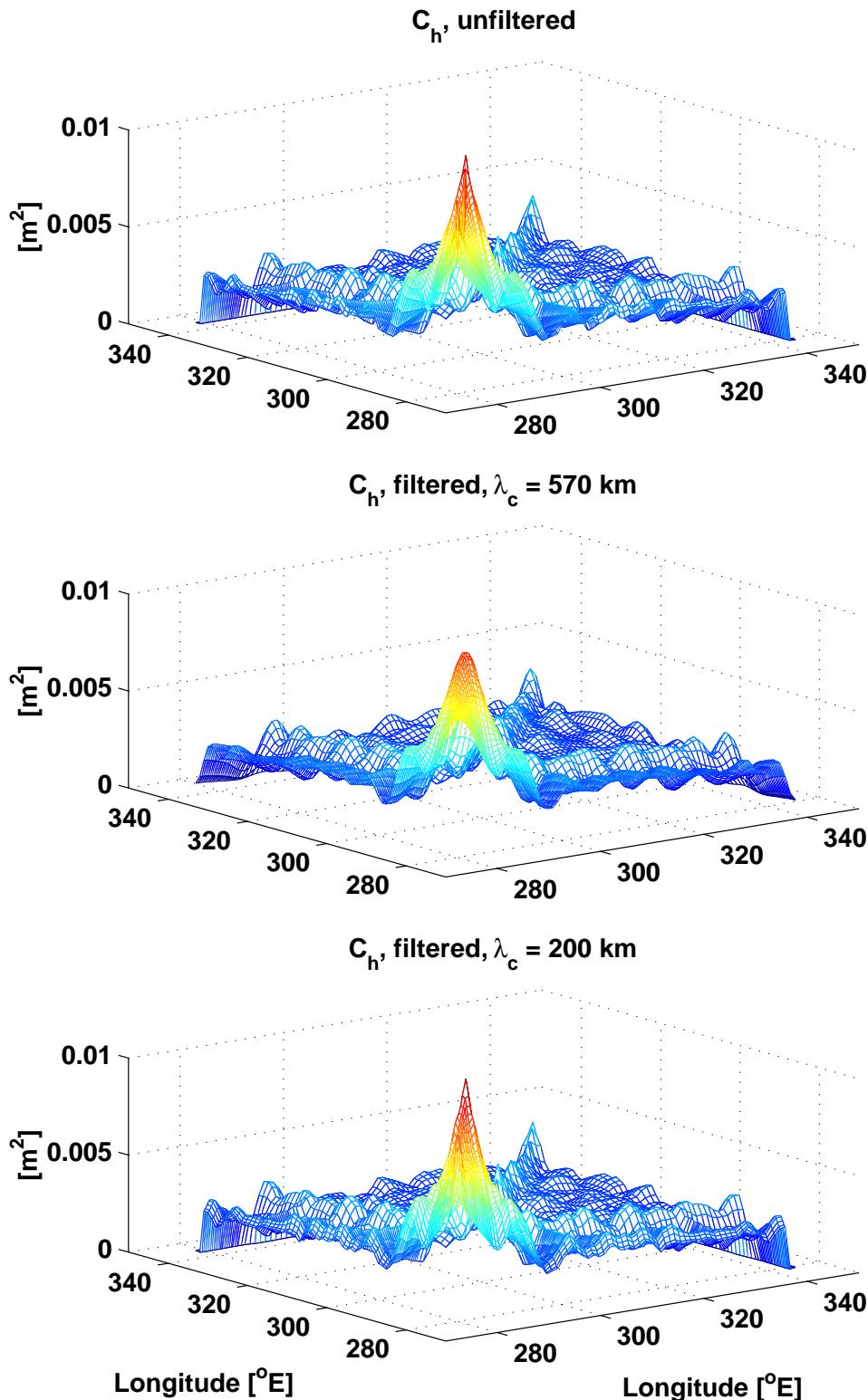
Figure 1. Total altimeter covariance $C_h = C_{fluc} + \chi$, for the North Atlantic hydrographic section along 24°N, unfiltered and filtered with two different cutoff wavelengths $\lambda_c = 570$ km and $\lambda_c = 200$ km. The section length is approximately 6600 km. For $\lambda_c = 200$ km, the filter results in only small changes to the covariance matrix C_h.
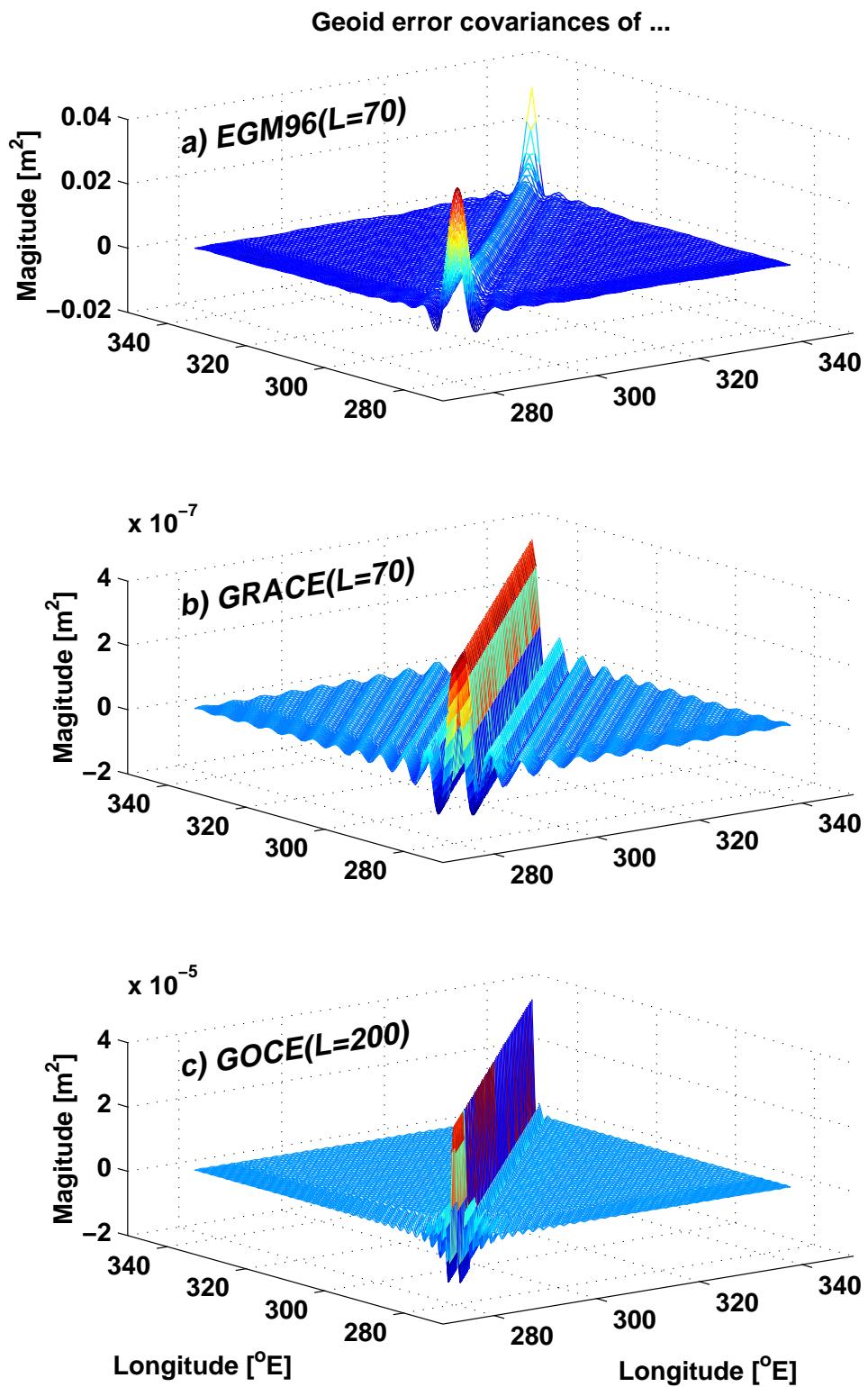
Figure 2. Geoid error covariance matrices to the degree and order L for a) EGM96, b) GRACE, and c) GOCE, for the North Atlantic section along 24°N.
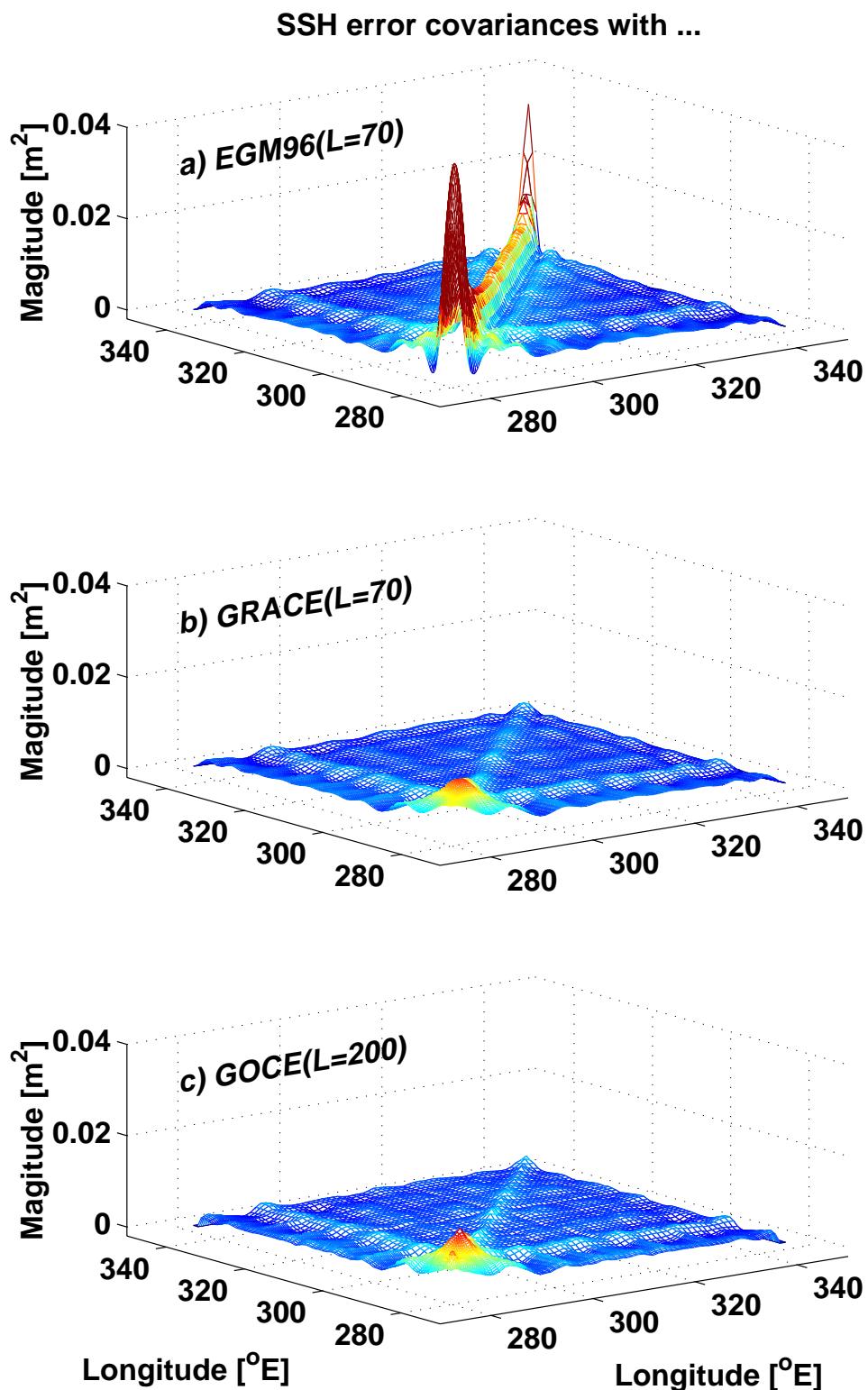
Figure 3. SSH error covariance matrices after filtering of all small scales according to the maximum degree and order used for a) EGM96, b) GRACE, and c) GOCE, for the North Atlantic section along 24°N.
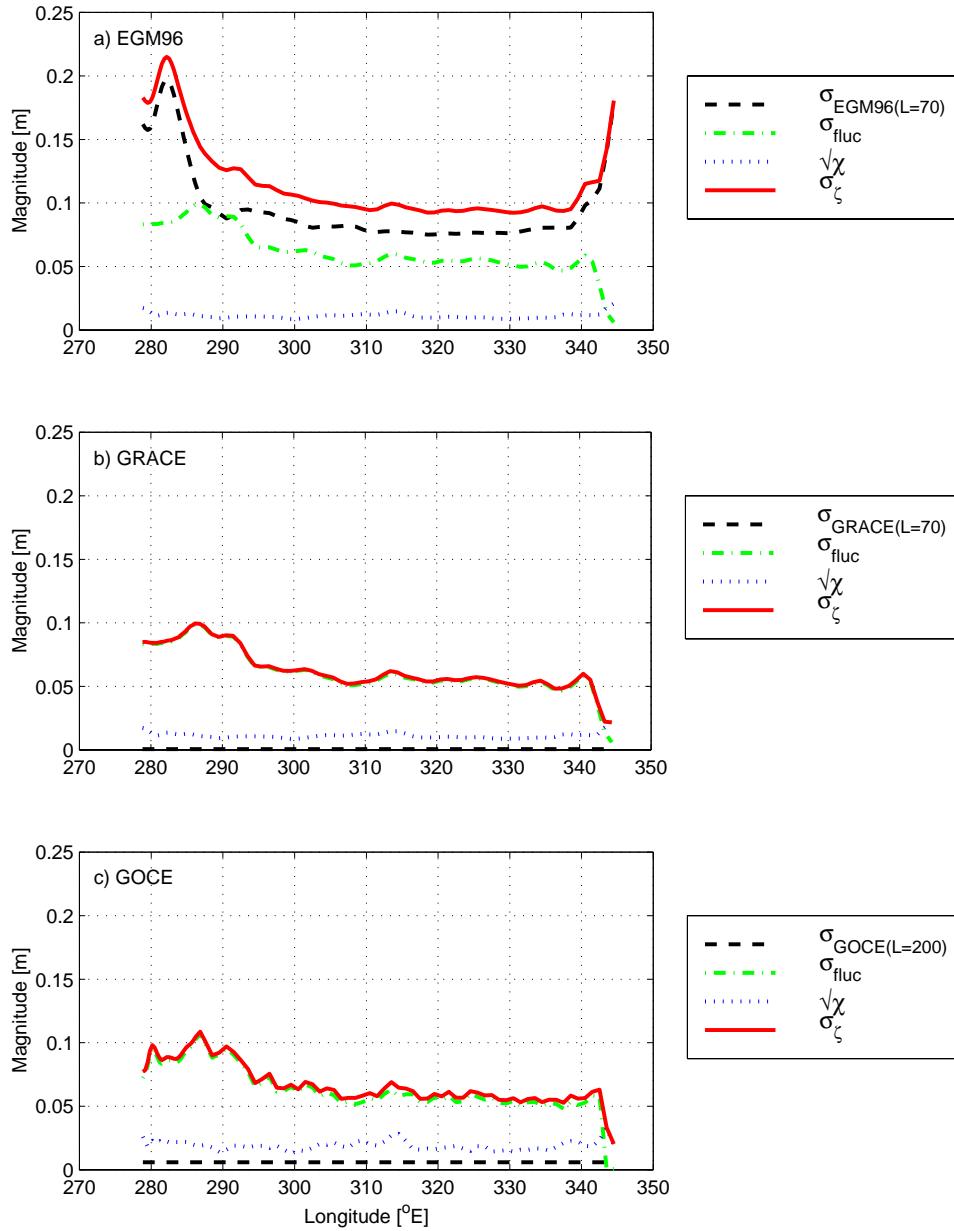
Figure 4. Square roots of the diagonals of the SSH error covariance matrices $\sigma_\zeta = \sqrt{\mathrm{diag}C_N + \mathrm{diag}C_{fluc} + \mathrm{diag}\chi}$ and their three constituents after filtering of the small scales according to the maximum degree and order used for a) EGM96, b) GRACE, and c) GOCE, for the North Atlantic section along 24°N. Note that the geoid contribution to the error is small for GRACE and GOCE.
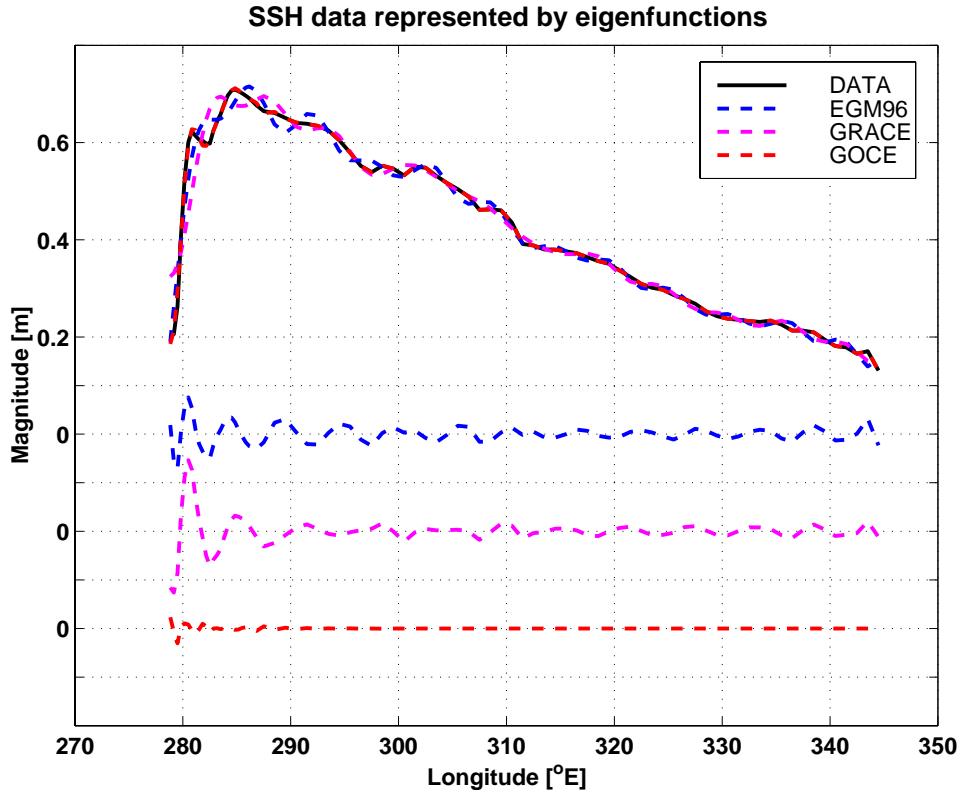
Figure 5. SSH data and its representation by an expansion in eigenvectors $\zeta^{(r)} = \sum \zeta_k \mathbf{v}_k$, where the sum is only taken over a meaningful subset of the eigenvector of the corresponding covariance matrix (see text), for the North Atlantic section along $24°$N. Also shown is the difference $\zeta^* - \zeta^{(r)}$. This part of the data is not resolved by the SSH representation and does not constrain the model solution.
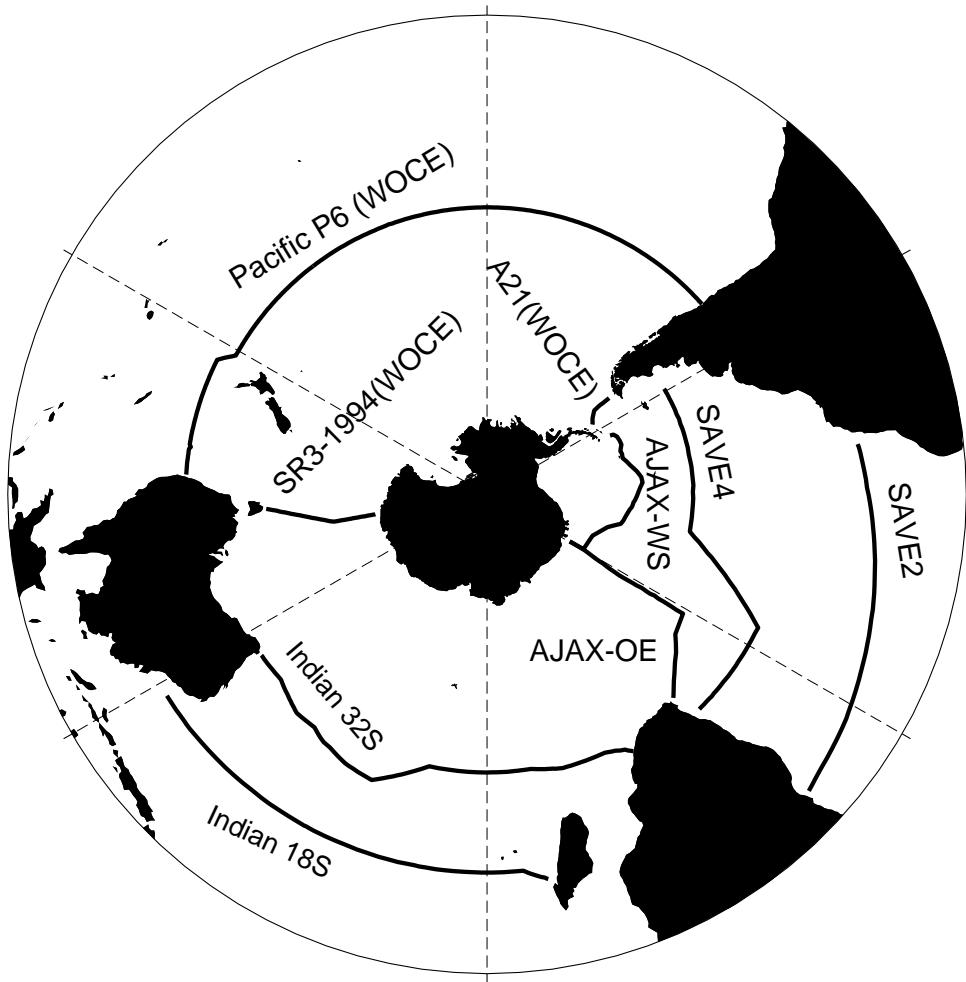
Figure 6. Position of hydrographic sections and box regions used in the inverse model.
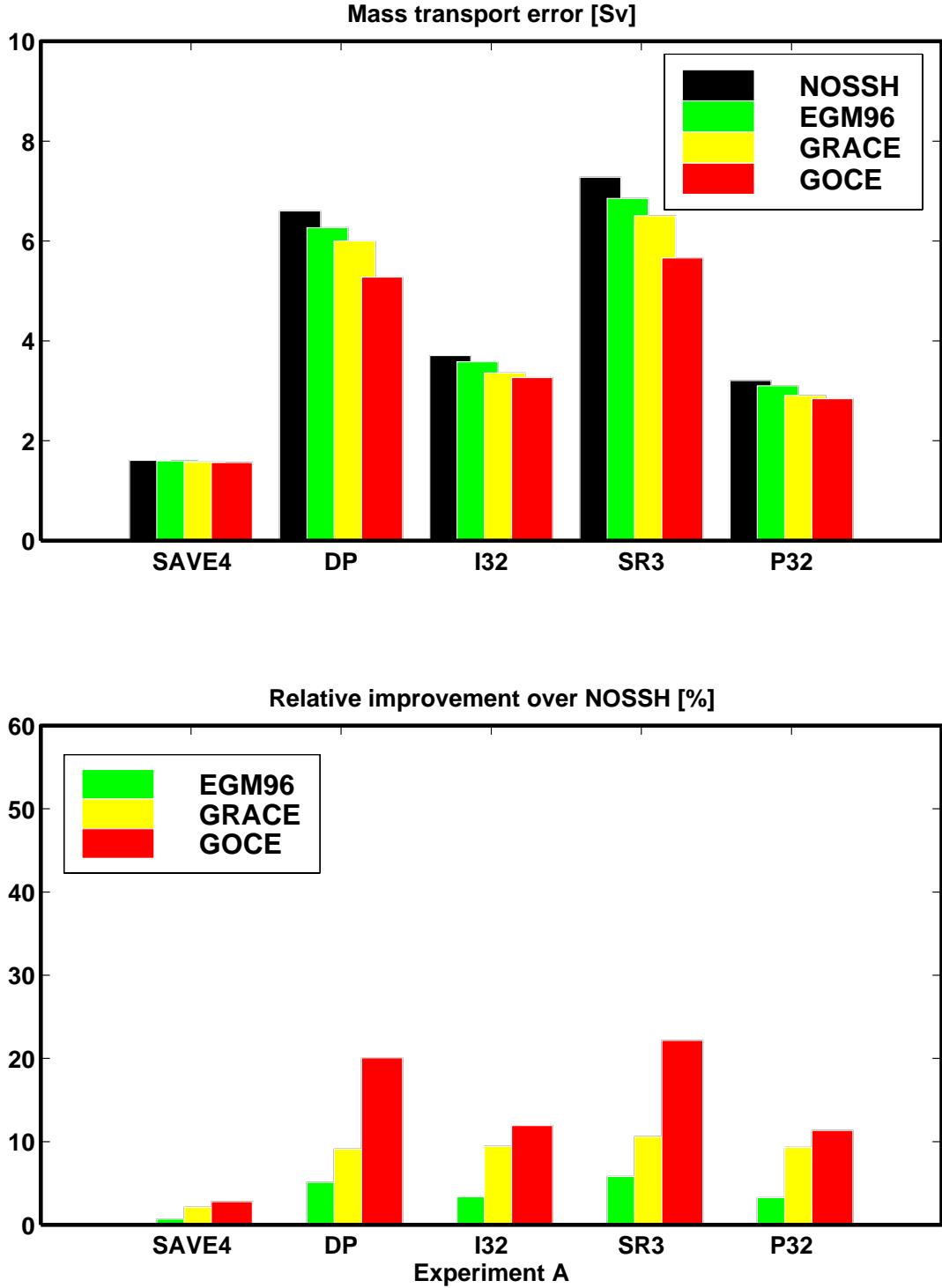
Figure 7. Impact of the different geoid error covariances in Experiment A on the accuracy of mass transports at selected sections. Upper panel is the mass error (Sv) and the lower panel is the percentage improvement of each geoid over the NOSSH solution. (1 Sv = 10^6 m^{3}s^{-1})
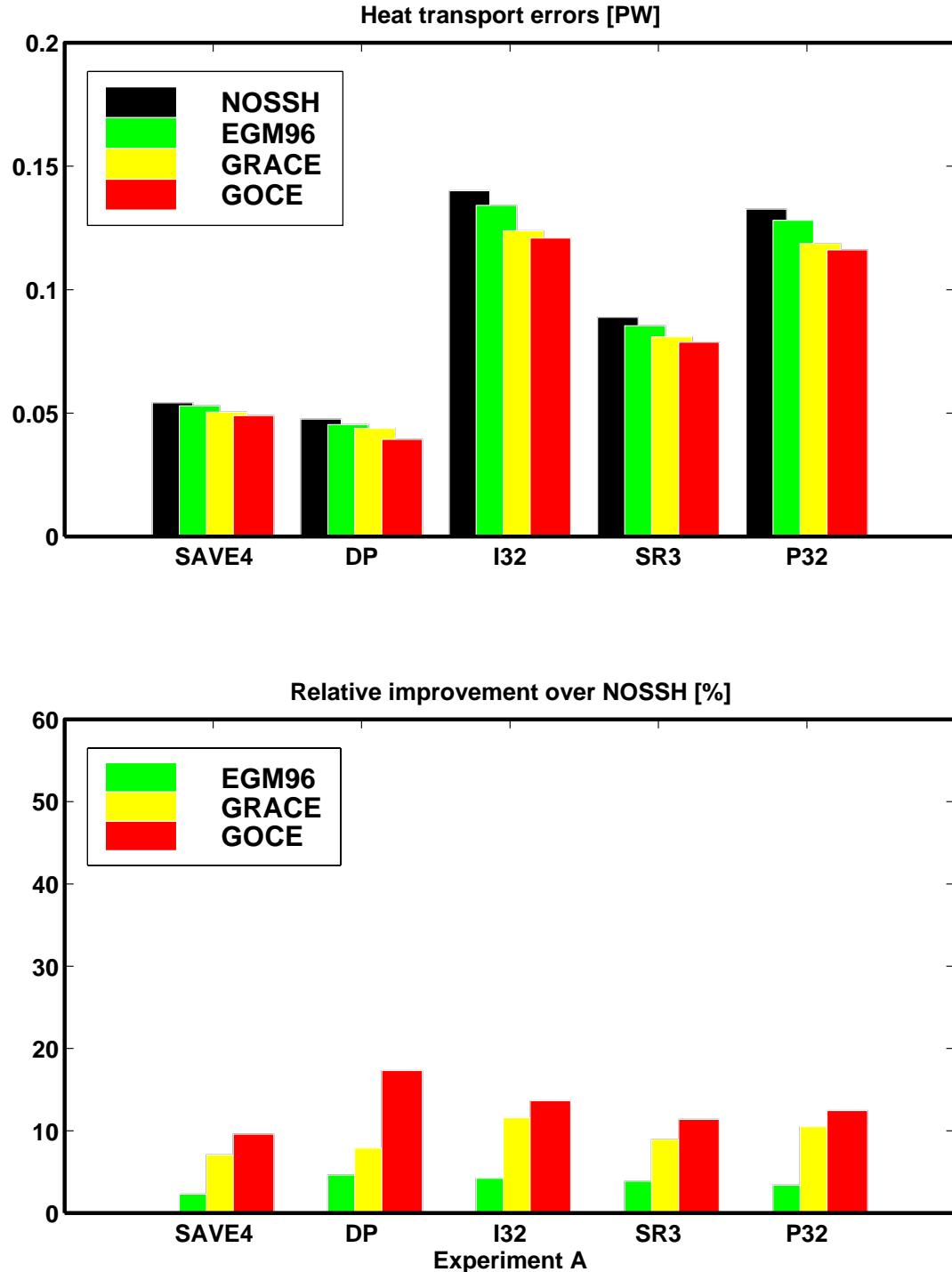
**Figure 8.** Impact of the different geoid error covariances in Experiment A on the accuracy of heat transports at selected sections. Upper panel is the heat transport error (PW) and the lower panel is the percentage improvement of each geoid over the NOSSH solution. (1 PW = 10^{15} Watts)
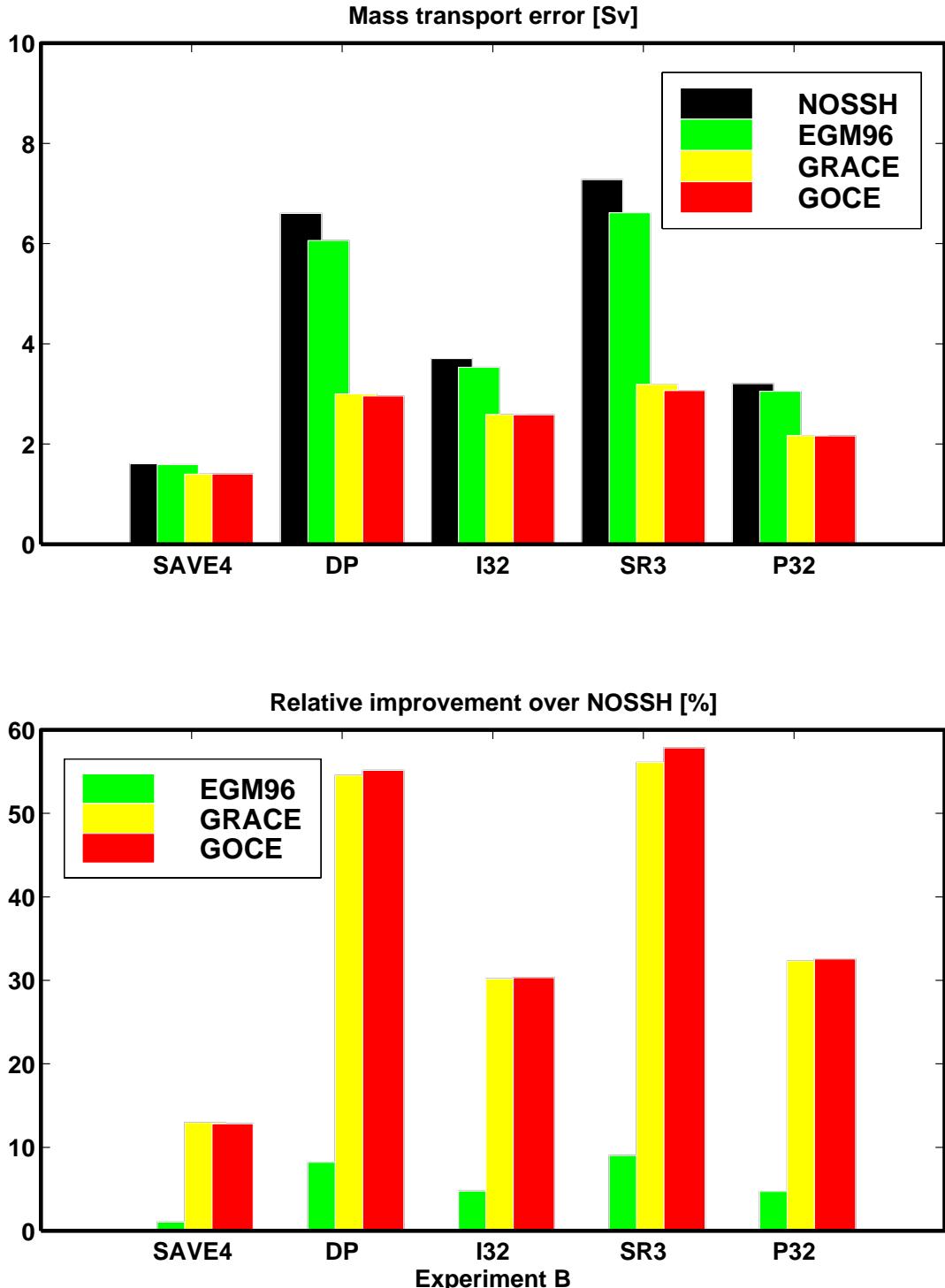
Figure 9. Impact of the different geoid error covariances in Experiment B (no error on SSH variability) on the accuracy of mass transports at selected sections. Upper panel is the mass error (Sv) and the lower panel is the percentage improvement of each geoid over the NOSSH solution.
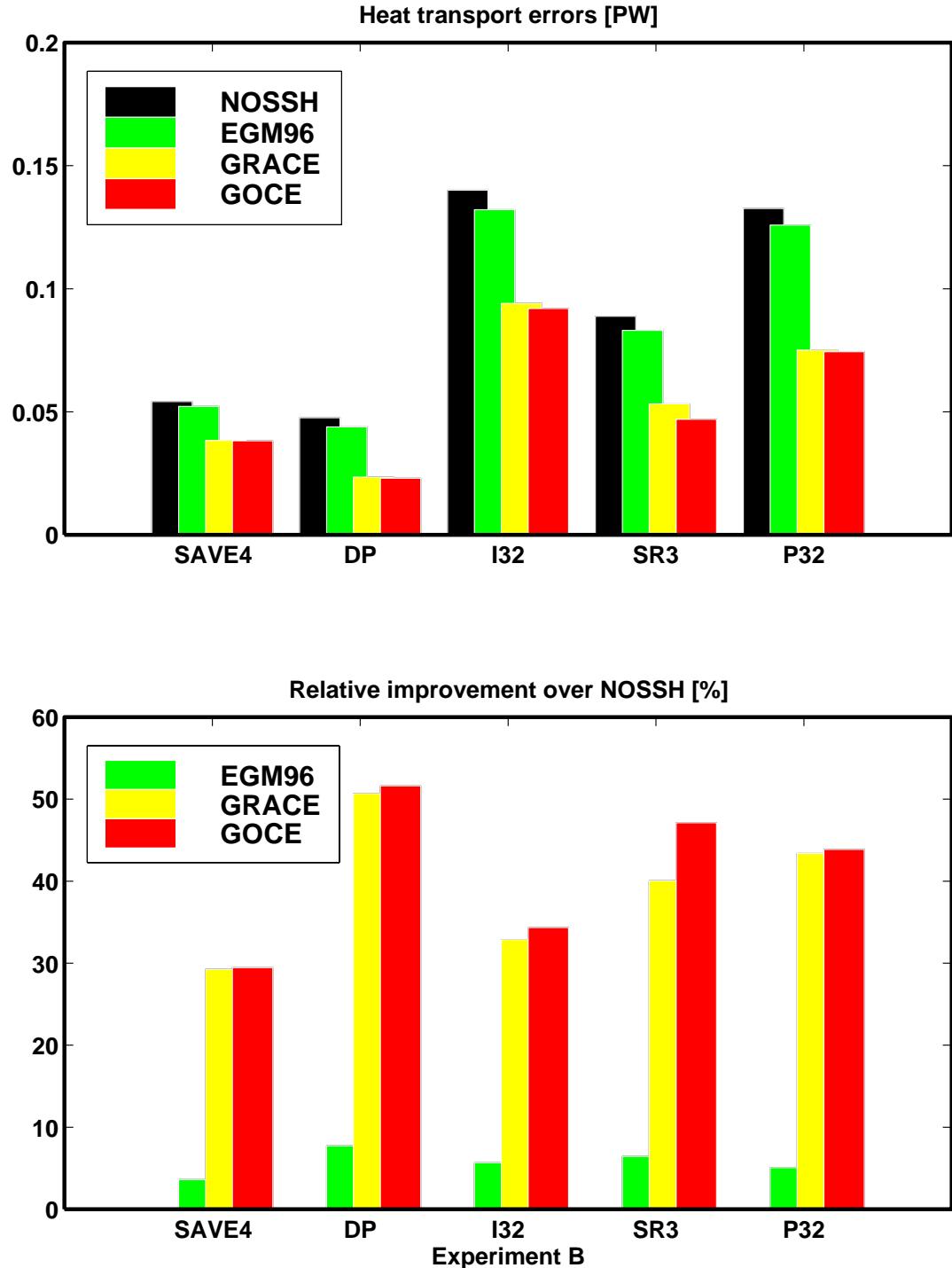
Figure 10. Impact of the different geoid error covariances in Experiment B (no error on SSH variability) on the accuracy of heat transports at selected sections. Upper panel is the heat transport error (PW) and the lower panel is the percentage improvement of each geoid over the NOSSH solution.
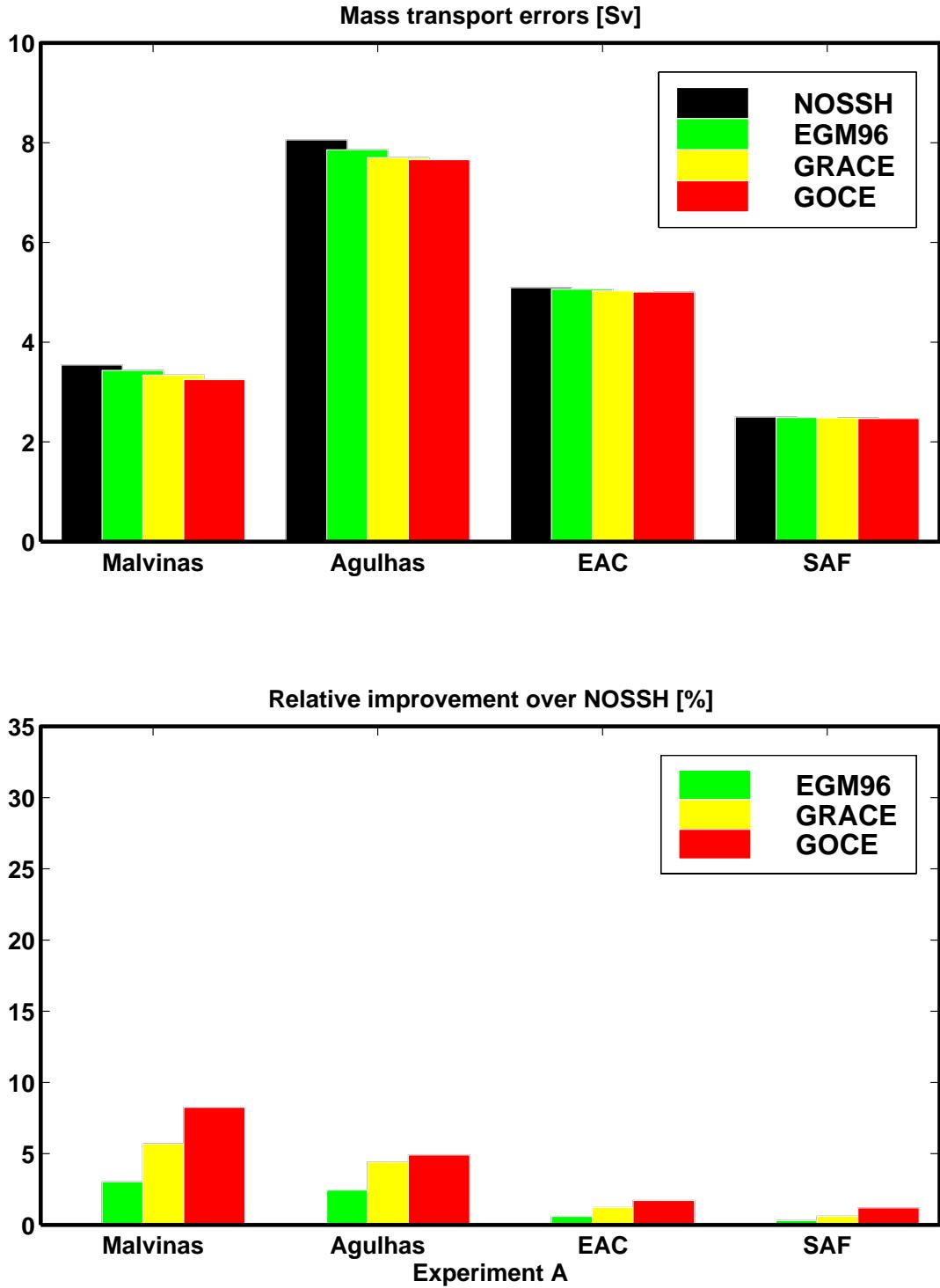
Figure 11. Impact of the different geoid models in Experiment A on the accuracy of mass transports at selected narrow currents of the Southern Ocean. Upper panel is the mass transport error (Sv) and the lower panel is the percentage improvement of each geoid model over the NOSSH solution. EAC: East Australian Current, SAF Sub-Antarctic Front.
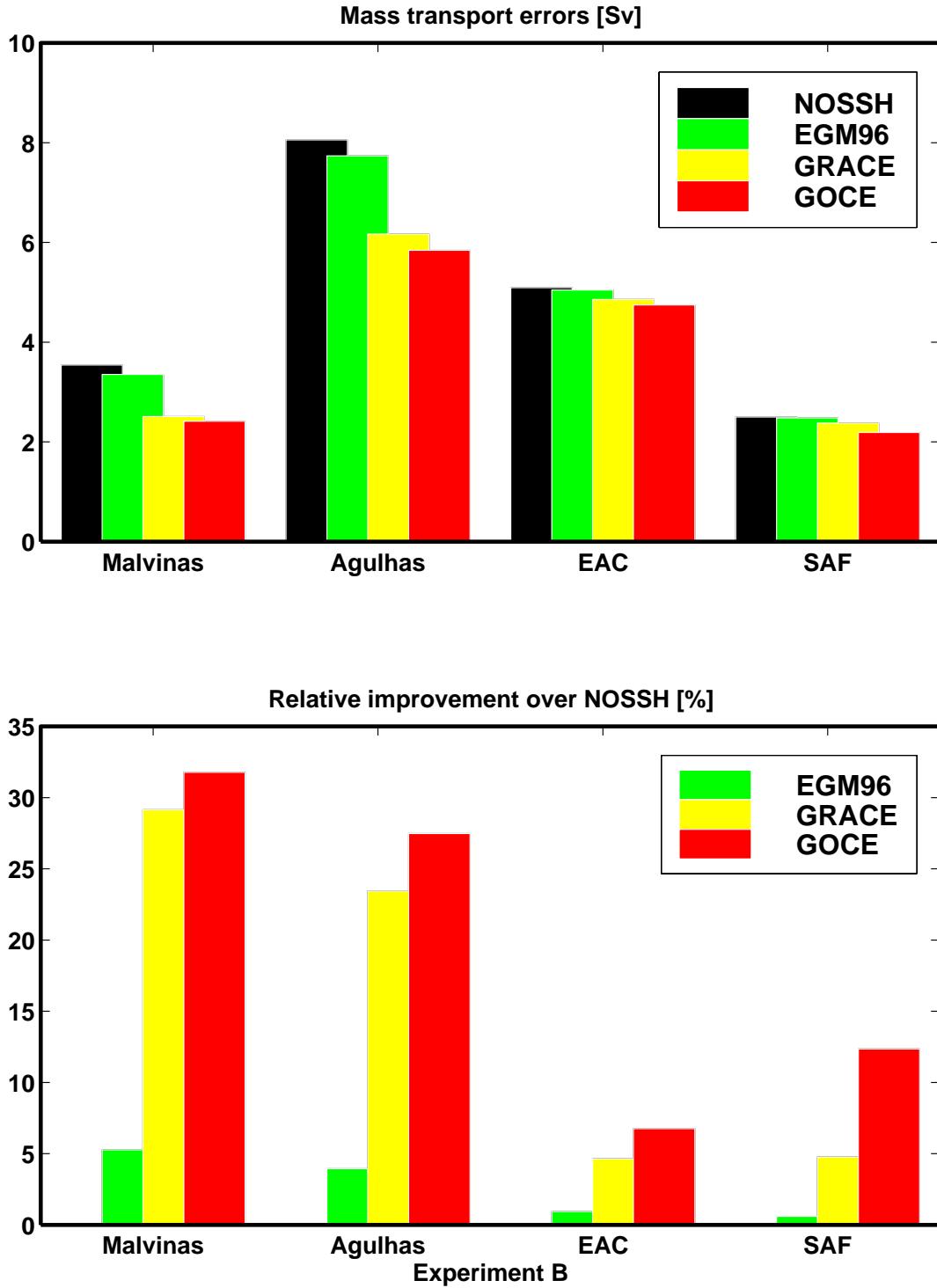
Figure 12. Impact of the different geoid models in Experiment B (no error on SSH variability)on the accuracy of mass transports at selected narrow currents of the Southern Ocean. Upper panel is the mass error (Sv) and the lower panel is the percentage improvement of each geoid model over the NOSSH solution. EAC: East Australian Current, SAF Sub-Antarctic Front.
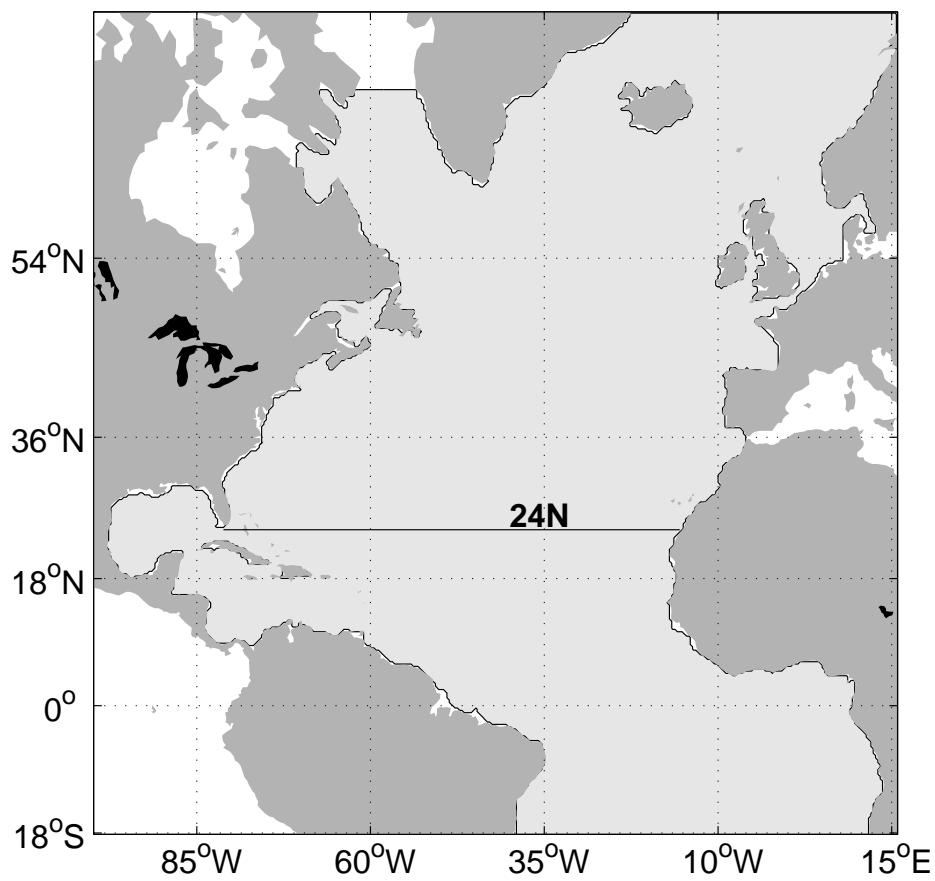
Figure 13. Model area of FLAME 1/3° North Atlantic Model (shaded area) and location of the "section" at 24°30'N.
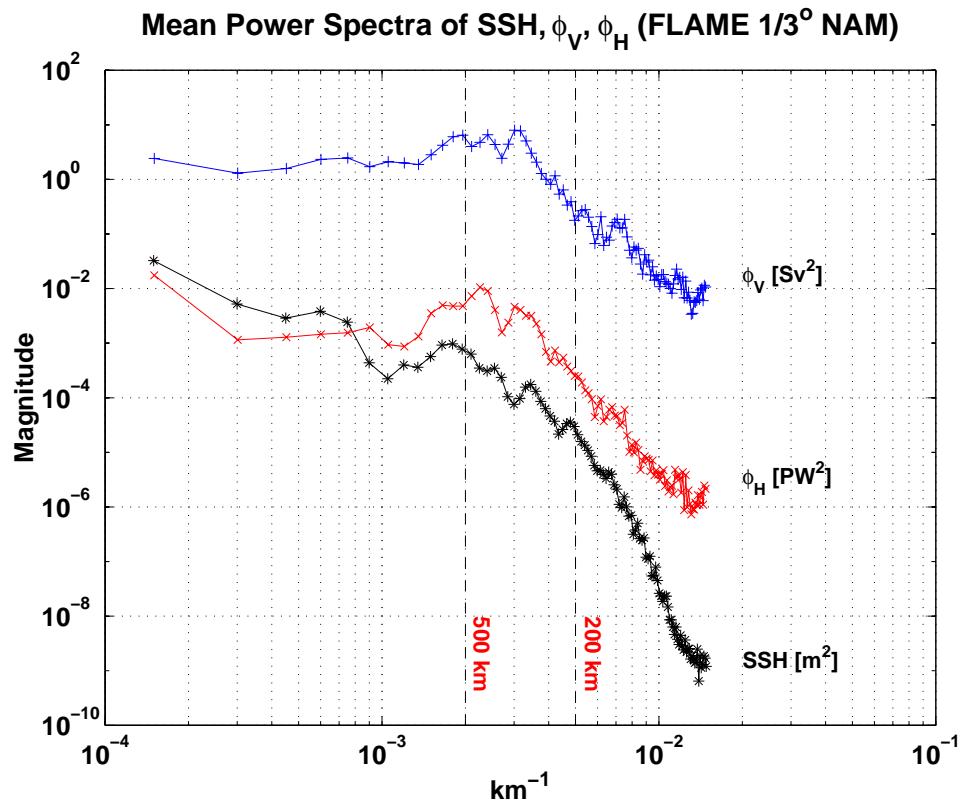
Figure 14. Power spectrum of SSH, mass tranport ϕ_V and heat transport ϕ_H at 24°30'N of FLAME 1/3° North Atlantic Model, one year record.
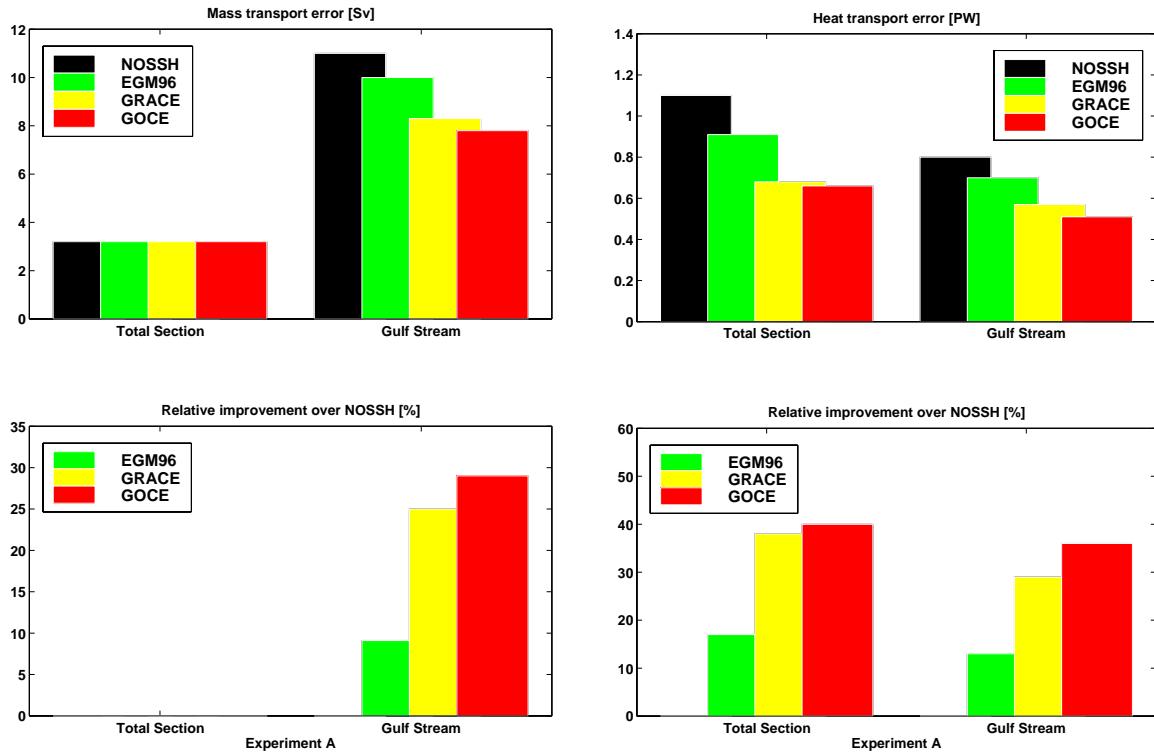
Figure 15. Impact of the different geoid models in Experiment A on the accuracy of the mass and heat transport across 24°N and the Florida Strait. Upper panel is the mass (Sv) and heat (PW) error and the lower panel is the percentage improvement of each geoid model over the NOSSH solution.
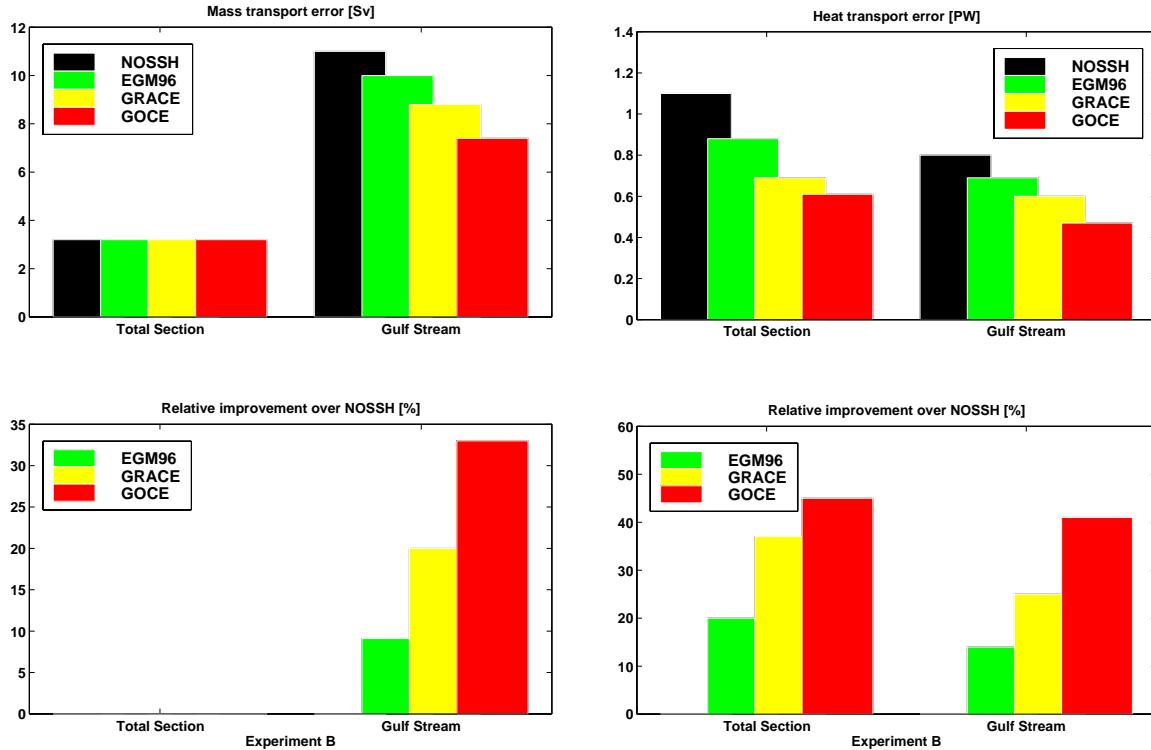
Figure 16. Impact of the different geoid models in Experiment B (no error on SSH variability) on the accuracy of the mass and heat transport across 24°N and the Florida Strait. Upper panel is the mass (Sv) and heat (PW) error and the lower panel is the percentage improvement of each geoid model over the NOSSH solution.
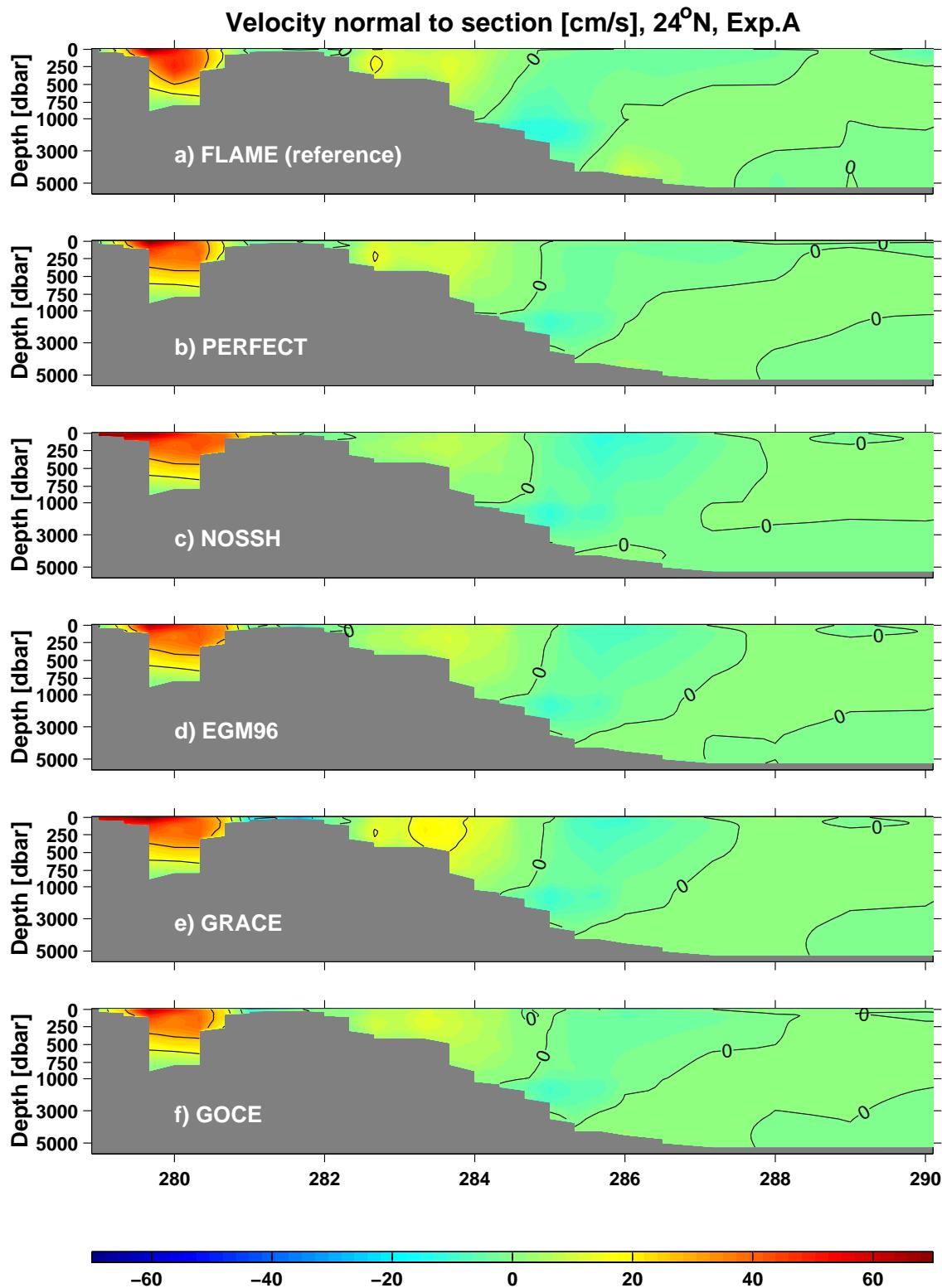
Figure 17. Comparison of velocity (cm/s) between the FLAME-"data" and the different model runs, for Experiment A, for the western end of the section. Note the stretched depth coordinate axis.
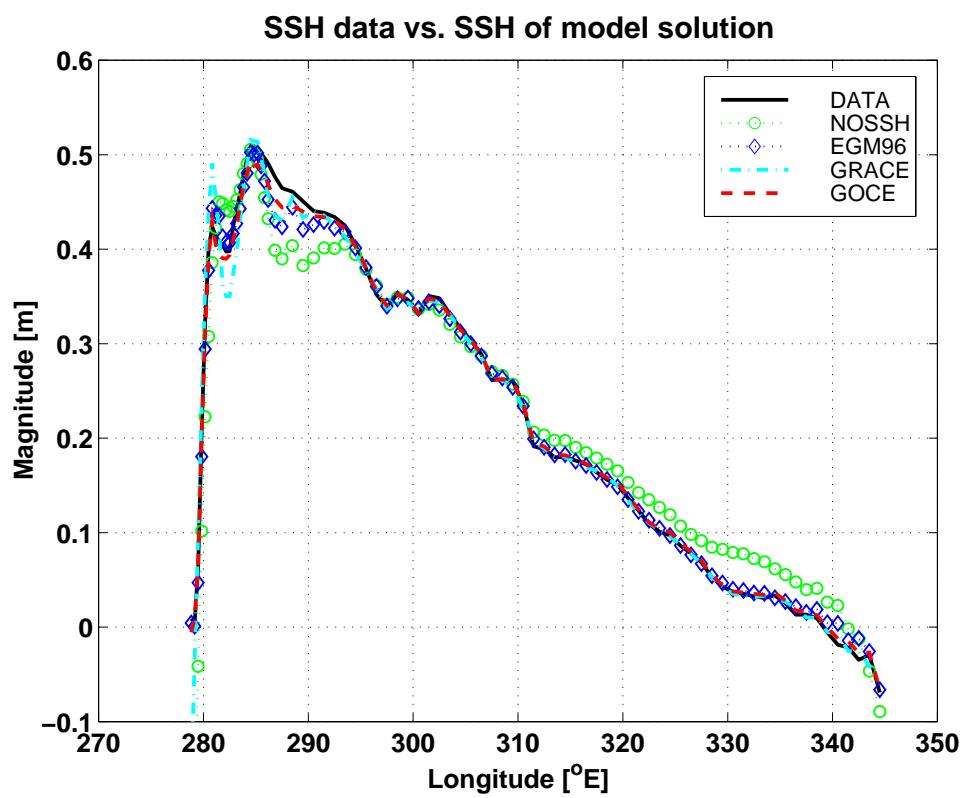
Figure 18. SSH of model runs vs. data, Experiment A
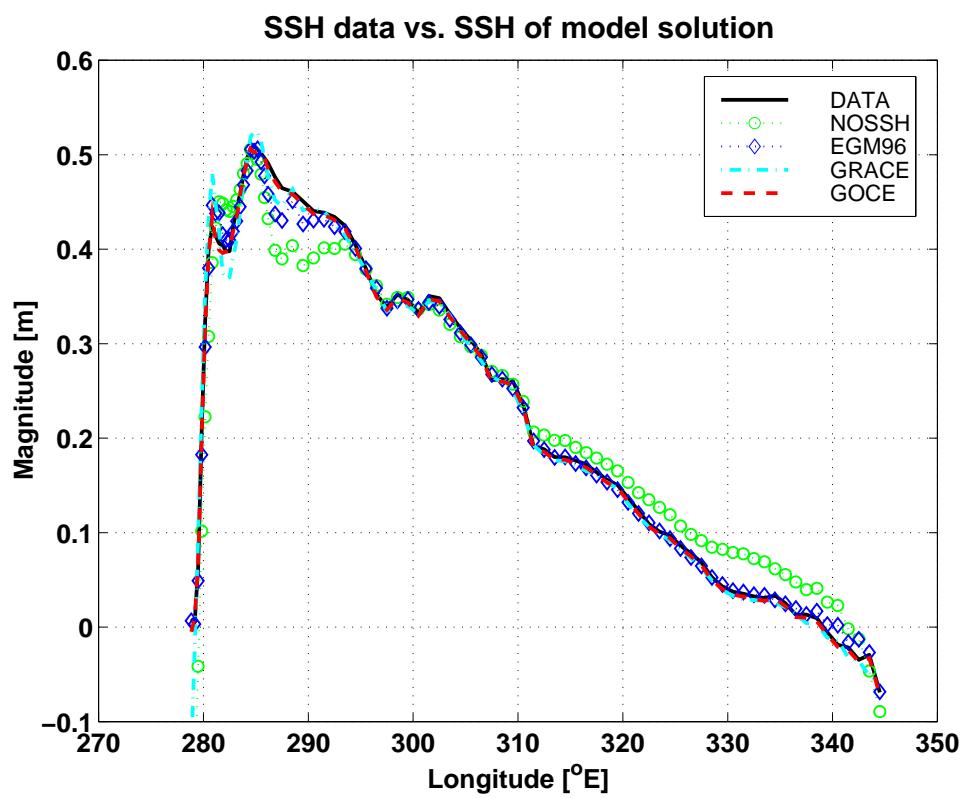
Figure 19. SSH of model runs vs. data, Experiment B (no error on SSH variability)

Tables

Sections		Year
SAVE 2 12°S	(SAVE2)	1988
SAVE 4 30°S – 47°S	(SAVE4)	1989
Drake Passage	(DP)	1990
AJAX-0°E	(SA)	1984
AJAX-Weddell Sea	(WS)	1984
Indian 18°S	(I18)	1976
Indian 32°S	(I32)	1987
WOCE-SR3 140°E	(SR3)	1994
WOCE-P6 32°S	(P32)	1992

Table 1. The hydrographic sections (and year) used in this study and abbreviated name used in the text.

Table 2. *A priori* constraints applied to the box-inverse model from independent ocean estimates. The inverse model conserves mass, heat and salt in all layers while silica is conserved in each box as a whole .

Constraint	
-0.4 ± 2Sv	net southward transport at SAVE2
4 ± 2Sv	northward bottom water transport in Brazil basin
0 ± 2Sv	net transport across Weddell Sea
$16 \pm 5\ Wm^{-2}$	heat loss over Weddell Sea
60 ± 5Sv	northward Malvinas Current
6 ± 2 Sv	northward transport AABW across Argentine basin
11 ± 5 Sv	northward transport LCDW/AABW coincident with WOCE PCM-9 (P32)
$O(500 kmols^{-1})$ Silica	Conservation all regions

Section	Mass [Sv]	Heat [PW]
SAVE2	-0.82 ± 0.39	0.49 ± 0.06
SAVE4	-0.31 ± 1.60	0.37 ± 0.05
DP	$137.5 \ \pm 6.6$	1.44 ± 0.05
SA	$138.5 \ \pm 7.0$	1.12 ± 0.09
WS	0.01 ± 0.20	-0.05 ± 0.004
I18	-7.40 ± 4.02	-1.28 ± 0.19
I32	-8.14 ± 3.71	-0.79 ± 0.14
SR3	$146.7 \ \pm 7.3$	1.72 ± 0.09
P32	7.31 ± 3.20	0.36 ± 0.13

Table 3. Total section property fluxes, heat fluxes are relative to 0°C.

	Total section				
	Geoid	ϕ_V [Sv]		ϕ_H [PW]	
control	DATA	0.1 ± 3.2		0.60 ± 0.10	
	NOSSH	0.1 ± 3.2		0.50 ± 1.1	
	PERFECT	0.0 ± 3.1	(3%)	0.46 ± 0.27	(75%)
Exp.A	EGM96	0.0 ± 3.2	(0%)	0.50 ± 0.91	(17%)
	GRACE	0.0 ± 3.2	(0%)	0.88 ± 0.68	(38%)
	GOCE	0.0 ± 3.2	(0%)	0.48 ± 0.66	(40%)
Exp.B	EGM96	0.0 ± 3.2	(0%)	0.50 ± 0.88	(20%)
	GRACE	0.0 ± 3.2	(0%)	0.60 ± 0.69	(37%)
	GOCE	0.0 ± 3.2	(0%)	0.47 ± 0.61	(45%)

	"Gulf Stream"				
	Geoid	ϕ_V [Sv]		ϕ_H [PW]	
control	DATA	26.0 ± 2.9		1.90 ± 0.20	
	NOSSH	30 ± 11		2.25 ± 0.80	
	PERFECT	25.3 ± 5.5	(50%)	1.85 ± 0.37	(54%)
Exp.A	EGM96	26 ± 10	(9%)	1.96 ± 0.70	(13%)
	GRACE	28.2 ± 8.3	(25%)	2.10 ± 0.57	(29%)
	GOCE	24.8 ± 7.8	(29%)	1.84 ± 0.51	(36%)
Exp.B	EGM96	26 ± 10	(9%)	1.97 ± 0.69	(14%)
	GRACE	27.3 ± 8.8	(20%)	2.03 ± 0.60	(25%)